Geovani Carvalho de Resende

Polarized Raman Spectroscopy in single layer $ReSe_2$

Dissertação apresentada ao Programa de Pós-Graduação em Física do Instituto de Ciências Exatas da Universidade Federal de Minas Gerais como requisito parcial para obtenção do título de Mestre em Física.

Supervisor: Marcos Assunção Pimenta

Co-supervisor: Bruno Ricardo de Carvalho

Belo Horizonte

2018

Fulano de
Modelo para teses e dissertações do departamento de Física da UFMG/ Fulano de . – Belo Horizonte, 2017-
59 p. : il. (algumas color.) ; 30 cm.

Orientador: Beltrano da Silva

Tese (Doutorado) – , 2017.

1. Palavra-chave1. 2. Palavra-chave2. 2. Palavra-chave3. I. Orientador. II. Universidade xxx. III. Faculdade de xxx. IV. Título

Fulano de Tal

Modelo para teses e dissertações do departamento de Física da UFMG

Tese apresentada ao Programa de Pós-Graduação em Física do Instituto de Ciências Exatas da Universidade Federal de Minas Gerais como requisito parcial para obtenção do título de Doutor em Ciências.

Trabalho aprovado. Belo Horizonte, 24 de novembro de 2012:

Beltrano da Silva
Orientador

Professor
Convidado 1

Professor
Convidado 2

Belo Horizonte
2017

Acknowledgements

Thanks God, for everything.

I am also very thankful to:

My dear boss Assunção Pimenta for the excellent masters supervision,for the physical discussion and for the conversations about life's ironies.

Bruno Ricardo de Carvalho, for the co-supervision that was also essential to solve many research and academic issues.

Cris Fantini, who helped me to understand much about the lab instrumentation, physics, experimental details and intimidated the tools to work properly.

The Chefa Ariete Righi, for the wisdom shared in dialogues and for not kicking me out of the group though I tested her patience many times.

All the Lab Raman for filling the work environment with joy and beer.

My mother for everything.

My dear, Jessica Santos Lemos.

Juliana Caldeira Brant, for the sample preparation.

My family.

My friends.

The Brazilian agencies CAPES, CNPq, INCT and FAPEMIG for funding this and many other scientific works in Brazil.

Resumo

A obtenção experimental do grafeno por Novoselov e Geim em 2004 abriu um horizonte de pesquisas em materiais bidimensionais. Estes materiais, por sua vez, apresentam um amplo leque de propriedades físicas desejáveis para aplicações em dispositivos eletrônicos, optoeletrônicos, spintrônicos, dentre outros. Portanto, os dicalcogenetos de metais de transição (TMDs, sigla do inglês Transition Metal Dichalcogenides) formam uma classe especial desses materiais, tendo em vista a riqueza das propriedades de seus membros, que variam de isolantes a supercondutores. O di-seleneto de rênio ($ReSe_2$) é um TMD semicondutor promissor para aplicações em eletrônica e optoeletrônica, não só pelo seu *band gap* no infravermelho, mas também devido às suas propriedades anisotrópicas oriundas de sua baixa simetria. Visto que o $ReSe_2$ é um dos TMDs menos conhecidos e que suas propriedades anisotrópicas necessitam ser entendidas minuciosamente para futuras aplicações tecnológicas, este trabalho visa um melhor entendimento das mesmas analisando o comportamento vibracional do material através de Espectroscopia Raman Polarizada. Assim, a dependência angular do espalhamento Raman de seus modos vibracionais é analisada segundo a teoria clássica para o espalhamento Raman. Além disso, é necessário levar em conta o efeito da diferença de fase entre as componenente independentes do tensor Raman para explicar os resultados experimentais obtidos para a maioria dos modos previstos por teoria de grupos.

Palavras-chave: dicalcogenetos de metais de transição, di-seleneto de rênio, espectroscopia Raman.

Abstract

The experimental isolation of graphene by Novoselov and Geim in 2004 opened a horizon in researches of bidimensional materials. These materials present a wide set of desirable physical properties for applications in electronic, optoecletronic, spintronic devices and others. Therefore, the transition metal dichalcogenides (TMDs) form a special class of materials, given the richness of the physical properties of their members, which vary from insulators to superconductors. Rhenium diselenide ($ReSe_2$) is a promising semiconductor TMD for electronic and optoelectronic applications, not only because of its band gap in infrared, but also because of its anisotropic properties that emerged from its low symmetry. Since $ReSe_2$ is one of the least known TMDs and its anisotropic properties need to be thoroughly understood for future technological applications, this work aims a better understanding of this material, analyzing its vibrational behaviour through Polarized Raman Spectroscopy. Then, the angular dependence of the Raman scattering is analyzed by the macroscopic theory of Raman scattering. Moreover, it is necessary to take into account the effect of the phase difference between independent Raman tensor elements to explain the experimental results obtained for most of the vibrational modes predicted by group theory.

Keywords: transition metal dichalcogenides, rhenium diselenide, Raman spectroscopy.

List of Figures

Figure 1 – **Building van der Waals heterostructures.** If one considers 2D crystals to be analogous to LEGO blocks 12
Figure 2 – **Structural polytypes of pristine semiconductor TMD layers.** Chalcogen atoms are shown in yellow 13
Figure 3 – **$ReSe_2$ crystal structure.** Selenium atoms are shown in yellow and rhenium atoms are shown in blue 14
Figure 4 – **The Raman scattering draft**. From left to right: the Stokes, Rayleigh and anti-Stokes peaks are represented 18
Figure 5 – **Feynman diagrams for one-phonon Stokes and anti-Stokes scattering.** (Right-side) Time evolution of 21
Figure 6 – **Polarized and Low-frequency Raman spectra of $ReSe_2$.** (a) Raman spectra of $ReSe_2$ as a function of the angle 24
Figure 7 – **Polar plots of bilayer $ReSe_2$** modes. Polar plots of the integrated Raman intensity of 25
Figure 8 – **Polar plots of bulk ReS_2.** Intensities as a function of angle with respect to the arbitrary laboratory x axis 26
Figure 9 – **Circularly polarized Raman spectra of ReS_2.** In red, the spectrum was recorded left-handed circularly polarized light 27
Figure 10 – **Micro-mechanical cleavage method.** Scheme of the steps done in the mechanical exfoliation to obtain single layers of 29
Figure 11 – **Low-frequency modes of $ReSe_2$.** (a) Raman spectra of the silicon substrate and the samples 30
Figure 12 – **Configurations of the spectrometer.** In the single mode, the light goes directly to the spectrograph 31
Figure 13 – **Experimental set up of our Raman laboratory.** The light is emitted by an Argon-Krypton laser source 32
Figure 14 – **Raman spectrum of single-layer $ReSe_2$.** Top: overall Raman spectrum of 1L-$ReSe_2$ recorded with a 2.33 eV excitation energy. 35
Figure 15 – **Polarized Raman spectra of a single-layer $ReSe_2$.** Raman spectra recorded in the parallel (Left) and crossed (Right) configurations 37
Figure 16 – **Angular dependence for Raman Tensor elements with real values.** Angular dependence of the 178.9 cm^{-1}, 251.1 cm^{-1} 38
Figure 17 – **Angular dependence of Raman intensities for real Raman Tensor values.** 40
Figure 18 – **Angular dependence of Raman intensities for complex Raman Tensor values.** 42

Figure 19 – **Polar plots of two $ReSe_2$ vibration modes.** Polar plots of the (a) 124.9 cm^{-1} and (b) 44
Figure 20 – **Polar plots of $ReSe_2$ vibration modes.**. olar plots of the (a) 124.9 cm^{-1} and (b) 46

List of abbreviations and acronyms

2D	Bidimensional
h-BN	Hexagonal Boron Nitride
TMDs	Transition Metal Dichalcogenides
CVD	Chemical Vapor Deposition
$ReSe_2$	Rhenium Diselenide
DFPT	Density Functional Perturbation Theory
CID	Circular Intensity Differential
N.A.	Numerical Aperture
CCD	Charge Cooled Device

Contents

1 INTRODUCTION 11
1.1 The two-dimensional layered materials 11
1.2 A brief review on $ReSe_2$ 12
1.3 Outline of this Master's Thesis 15

2 THEORY OF RAMAN SCATTERING 16
2.1 The classical approach 16
2.2 The microscopic treatment 20
2.3 Raman Spectroscopy on Re-based TMDs 22

3 EXPERIMENTAL METHODS 28
3.1 Sample preparation 28
3.2 Sample characterization 29
3.3 Instrumentation 30

4 RESULTS AND DISCUSSION 34
4.1 Raman-active modes 34
4.2 Polarized Raman Spectroscopy 36
4.3 Conclusion 44

5 CONCLUSION AND PERSPECTIVES 48

BIBLIOGRAPHY 50

1 Introduction

In this chapter, we present a brief review of the scientific context in which our work is inserted. We start on the flashpoint that boosted several works in Solid State Physics in this century: the experimental isolation of the graphene. Some classes of two-dimensional materials and their applications are discussed. Then, we introduce rhenium diselenide, the material investigated in this work, providing a short description of its properties. Finally, we present our objectives and the structure of this Master's thesis.

1.1 The two-dimensional layered materials

The experimental isolation of graphene in 2004 from a graphite crystal [1] paved the way for scientists to explore a new class of physical systems. This new class is composed of two-dimensional (2D) materials such as graphene itself, hexagonal boron nitride (h-BN) and transition metal dichalcogenides (TMDs) among others. These 2D materials show a large diversity of physical properties [2] and can be even more striking due to the possibility of stacking layers of different 2D materials forming heterostructures, as illustrated in Figure 1. This stacking procedure is like playing LEGO on an atomic scale and enable us to create atomically thin devices [3]. Such diversity indicates the necessity to understand these systems for future applications and boosted research in solid-state physics.

Due to the great variety of different combinations that the TMDs offer, they are the target material for electronic, optoelectronic, spintronic and valleytronic devices [2]. They form a class of around sixty members, where two-thirds of them assume layered structures [4]. It means that there are about forty types of TMD materials where a single-layer structure can be isolated by the micro-mechanical cleavage technique [5]. Moreover, theoretical studies predict that there are even more potentially exfoliable layered compounds [6]. Unlike graphene, whose monolayer is composed by a single plane of carbon atoms, the crystalline structure of TMDs is formed by three atomic layers in a $X - M - X$ (or MX_2) arrangement, where M represents the transition metal (*e.g.*, $M = Mo, W, Re$) and X the chalcogen atom (*e.g.*, $X = S, Se, Te$), as shown in Figure 2. Depending on the combination of the transition metal and the chalcogen atom, the TMDs can be either insulating, semiconducting, metallic or even magnetic [2, 4, 5, 7–9].

Although TMD crystals have been extensively studied in the past [4], only recently single- and few-layers have been obtained and explored [10–12]. This has been achieved due to the development of the micro-mechanical cleavage technique [10], and other methods such as the chemical vapor deposition (CVD) [13] and chemical exfoliation [14]. The

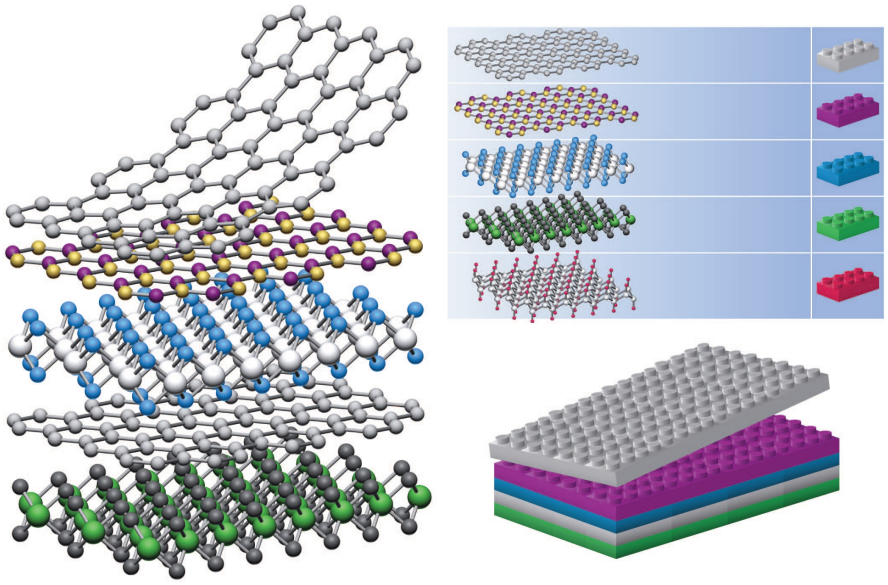

Figure 1 – **Building van der Waals heterostructures.** If one considers a 2D crystal to be analogous to LEGO blocks (right-side panel), the construction of a huge variety of layered structures becomes possible. Conceptually, this atomic-scale LEGO resembles molecular beam epitaxy but employs different "construction" rules and a distinct set of materials. Taken from reference [3].

TMD materials, upon the reduction of their thickness, have considerable changes in their electronic and vibrational properties [15, 16], in addition to the effects induced by the symmetry breaking [12, 17]. For example, in the case of semiconducting TMDs such as MoS_2 and WS_2, there is a transition from indirect to direct band gap as their layer thickness decreases from bulk and few-layers to a single atomic layer [11, 12]. Therefore, this indirect-to-direct band gap transition along with the strong spin-orbit coupling present in these materials [18] contributes to the understanding of the solid state physics underlined in these 2D systems, providing a better understanding of their diverse physical properties. Additionally, it opens up a new route of applications in optoelectronic and valleytronic (the study of the spin in the valley) devices [12].

Semiconducting TMDs such as MoS_2, $MoSe_2$, WS_2 and WSe_2 have drawn attention of most studies in 2D TMDs. Their basic optical and vibrational properties [11, 19] show prodigious applications for transistor and photodetector productions [20, 21]. However, it is in the same scenario of promising applications for the production of new devices that a special TMD named as rhenium diselenide ($ReSe_2$) arises.

1.2 A brief review on $ReSe_2$

Nowadays, rhenium diselenide ($ReSe_2$) is one of the least known 2D systems though there are already some reports on its applications for photodetectors and transistors [23, 24]. It has also been observed that $ReSe_2$ physical properties can be tuned by local strain

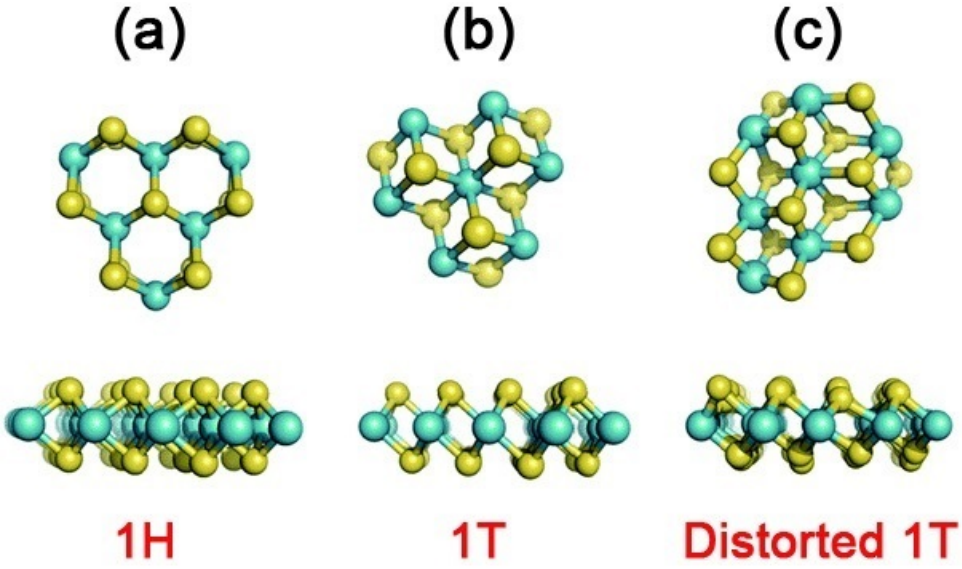

Figure 2 – **Structural polytypes of pristine semiconductor TMD layers.** Chalcogen atoms are shown in yellow, and transition metal atoms are shown in blue. (a) The 1H phase, (b) the 1T phase, (c) the distorted 1T, or 1T′ phase. First row shows the top view of the layer plane while second row shows the lateral view of the layer plane. Taken and adapted from reference [22].

generated by wrinkles [25]. Local strain produces a red shift in its photoluminescence peak, enhances its light emission, induces magnetism and modulates its electrical properties, for example, changing its electrical resistivity [25]. Unlike other semiconducting TMDs, which crystallizes in the trigonal prismatic phase (1H, see Figure 2 (a)), $ReSe_2$ (and its analogue, ReS_2) crystallizes in the distorted octahedral phase (1T', see Figure 2 (c)) possessing a triclinic symmetry that grants anisotropic properties to $ReSe_2$ [26]. Additionally, $ReSe_2$ remains an indirect semiconductor with a 1.32 eV gap in its single-layer form [27]. Contrarily to the semiconducting TMDs (e.g., MoS_2) that possess only 3 atoms per unit cell [4], it has a large unit cell composed by 12 atoms (see Figure 3) of which 4 are rhenium atoms and 8 are selenium atoms and presents diamond-shaped metal-metal bonds that form quasi-one-dimensional rhenium chains, as shown in Figure 3 (e), apart from the metal-chalcogen bonds. [4, 28, 29]

An interesting mark of the Re-TMDs is that they belong to the low symmetry C_i point group. This point group only has the identity and inversion symmetry elements and, for Re-TMDs, all the atoms of their unit cell are displaced from the inversion center [26,30]. Their Raman spectra have 18 first-order non-degenerate vibrational modes that belong to the irreducible representation A_g (totally symmetric) [26, 30]. Moreover, the intensities of these modes show strong angular dependence due to the reduced symmetry, as reported for monolayer [26, 27] and fewlayers $ReSe_2$ [27, 30].

However, the experimental methodology used to investigate the angular dependence of the Raman response of monolayer $ReSe_2$ in references [26] and [27] may not be the most

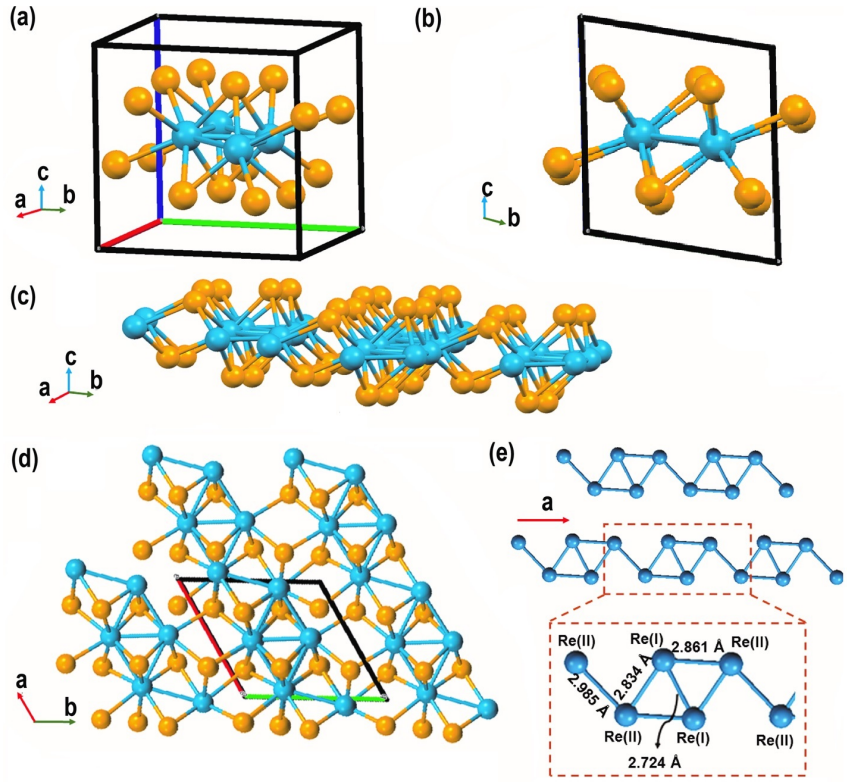

Figure 3 – **$ReSe_2$ crystal structure.** Selenium atoms are shown in yellow and rhenium atoms are shown in blue. (a) Schematic view of $ReSe_2$ unit cell. (b) projection of the unit cell in the *bc*-plane. (c) illustration of a $ReSe_2$ layer. (d) top view of the $ReSe_2$ layer highlighting the unit cell and the a and b lattice vectors. (e) scheme of the diamond-shaped Re-chains showing the Re-Re bond lengths. Taken and adapted from reference [29].

appropriate one, because it can lead to an incomplete or even wrong value of the Raman tensor elements. Such aspects will be discussed later in this Master's thesis.

In this work, we have performed a set of polarized Raman measurements on monolayer $ReSe_2$ using a more accurate method to probe its vibrational and optical properties. Differently from previous works [26, 27], we have implemented a series of polarized Raman measurements using an analyzer placed before the spectrograph entry. In addition to that, for a set of measurements, we also used a half-wave plate to rotate the incident light polarization by 90 degrees with respect to the analyzer axis. Then, we compared our results with previous reports in the literature and discussed the anisotropy and phase difference between independent Raman tensor elements effects based on the Raman scattering theory. Additionally, based on the outcomes and implications of our results, we also present perspectives of future works to further probe the electronic and vibrational properties of $ReSe_2$ from single-layer, few-layers to the bulk material. Our results may also be applied to other similar Re-TMDs materials.

1.3 Outline of this Master's Thesis

To accomplish the objectives previously mentioned, this Master's Thesis is organized as follows:

- CHAPTER 2, we discuss about the theory of Raman scattering;
- CHAPTER 3, we discuss the experimental methodology employed in our work, in particular, the sample preparation and the polarized Raman spectroscopy setup.
- CHAPTER 4, we present our results and discuss their implications.
- CHAPTER 5, we finish our discussions and present perspectives of future works.

2 Theory of Raman Scattering

When light interacts with matter, a small portion of the light can be inelastically scattered while this process creates or annihilates a quantum (or quanta) of vibration(s). This phenomenon was first observed in 1928 [31] and bears the name of its discoverer, Sir Chandrasekhara Venkata Raman, who two years later of the discovery was awarded the Nobel Prize in Physics [32].

In the early 1960's, many developments in the optical field of Raman instrumentation took place. For instance, the implementation of laser sources to record the Raman spectrum, holographic gratings, triple monochromator systems, and several others. These progresses resulted in resurgence in the use of the original Raman effect which helped physicists and chemists to further probe the vibrational and electronic properties of matter [33].

In this chapter, we present the theory of the Raman scattering effect. We start with the classical approach, the main theory used to explain our results. Then, we discuss the quantum model approach that allows us to understand the Raman scattering on the atomic scale. Finally, we review the state-of-art on Raman spectroscopy in rhenium dichalcogenides, highlighting how the anisotropic vibrational and optical properties have been explained thus far in the literature.

2.1 The classical approach

Consider a light of frequency ω_0 described, for simplicity, by a plane electromagnetic field as follows:

$$\mathbf{E}(\mathbf{r},t) = \mathbf{E}_0 \cos(\mathbf{k}_0 \cdot \mathbf{r} - \omega_0 t) \tag{2.1}$$

When the electromagnetic field interacts with a medium of electric susceptibility tensor $\overleftrightarrow{\chi}$, it induces an electric polarization vector $\mathbf{P}(\mathbf{r},t)$ such that:

$$\mathbf{P}(\mathbf{r},t) = \overleftrightarrow{\chi} \cdot \mathbf{E}(\mathbf{r},t) \tag{2.2}$$

Notice that $\overleftrightarrow{\chi}$ is a function of the frequency of incident radiation, $\overleftrightarrow{\chi}(\omega_0)$. The susceptibility tensor also depends on the atomic displacements caused by thermally excited atomic vibrations [34]. Let $\mathbf{Q}^k(\mathbf{r},t)$ be the normal coordinate corresponding to one of these atomic vibrations and the medium be a crystal[1]. Thus, in the regime of small oscillations, $\mathbf{Q}^k(\mathbf{r},t)$

[1] In the quantum formalism, $\mathbf{Q}^k(\mathbf{r},t)$ is the atomic displacement associated with a quantum of vibration of this crystal, i.e. a phonon with a momentum $\mathbf{q}$ and frequency ω.

can be expressed as a harmonic oscillation around an equilibrium position $\mathbf{Q}_0$ described as:

$$\mathbf{Q}^k(\mathbf{r},t) = \mathbf{Q}_0(\mathbf{q},\omega)\cos(\mathbf{q}\cdot\mathbf{r}-\omega t) \tag{2.3}$$

For small vibration amplitudes, the electric susceptibility tensor can be expanded in a Taylor series in $\mathbf{Q}^k(\mathbf{r},t)$ as:

$$\overleftrightarrow{\chi}(\omega_0,\mathbf{Q}^k) = \overleftrightarrow{\chi}_0(\omega_0) + \left(\frac{\partial\overleftrightarrow{\chi}}{\partial\mathbf{Q}^k}\right)\Bigg|_{\mathbf{Q}_0}\mathbf{Q}^k(\mathbf{r},t) + ... \tag{2.4}$$

Thus, substituting the expression above in (2.2) and keeping just terms up to the first the order, we find

$$\mathbf{P}(\mathbf{r},t,\mathbf{Q}^k) \approx \mathbf{P}_0(\mathbf{r},t) + \mathbf{P}_{vib}(\mathbf{r},t,\mathbf{Q}^k), \tag{2.5}$$

where

$$\mathbf{P}_0(\mathbf{r},t) = \overleftrightarrow{\chi}_0(\omega_0)\mathbf{E}_0\cos(\mathbf{k}_0\cdot\mathbf{r}-\omega_0 t) \tag{2.6}$$

represents a polarization vector oscillating with the same frequency of the incident radiation. This term is responsible for the elastic scattering of the incident beam, known as Rayleigh scattering, as depicted in Figure 4.

The term,

$$\mathbf{P}_{vib}(\mathbf{r},t,\mathbf{Q}^k) = \left(\frac{\partial\overleftrightarrow{\chi}}{\partial\mathbf{Q}^k}\right)\Bigg|_{\mathbf{Q}_0}\mathbf{Q}^k(\mathbf{r},t)\mathbf{E}_0\cos(\mathbf{k}_0\cdot\mathbf{r}-\omega_0 t) \tag{2.7}$$

is the polarization wave modulated by the vibration. To examine the frequency and wavevector of the radiation emitted by $\mathbf{P}_{vib}$, we substitute (2.3) in (2.7) and rearranging the terms, we find

$$\mathbf{P}_{vib}(\mathbf{r},t,\mathbf{Q}^k) = \frac{1}{2}\left(\frac{\partial\overleftrightarrow{\chi}}{\partial\mathbf{Q}^k}\right)\Bigg|_{\mathbf{Q}_0}\mathbf{Q}_0(\omega)\mathbf{E}_0\times \\ [\cos((\mathbf{k}_0+\mathbf{q})\cdot\mathbf{r}-(\omega_0+\omega)t) + \cos((\mathbf{k}_0-\mathbf{q})\cdot\mathbf{r}-(\omega_0-\omega)t)]. \tag{2.8}$$

Thus, from the expression in the square brackets, we notice that the polarization $\mathbf{P}_{vib}$ is composed by two terms that produces radiation with frequencies: (i) $\omega_{AS} = \omega_0 + \omega$, higher frequency than the incident light; and (ii) $\omega_S = \omega_0 - \omega$, lower frequency than the incident light. Therefore, the polarization modulated by vibration gives rise to the Raman

scattering effect. The emission of light with frequency ω_{AS} corresponds to the anti-Stokes scattering, whereas ω_S corresponds to the Stoke scattering [33, 34]. These processes are illustrated in Figure 4.

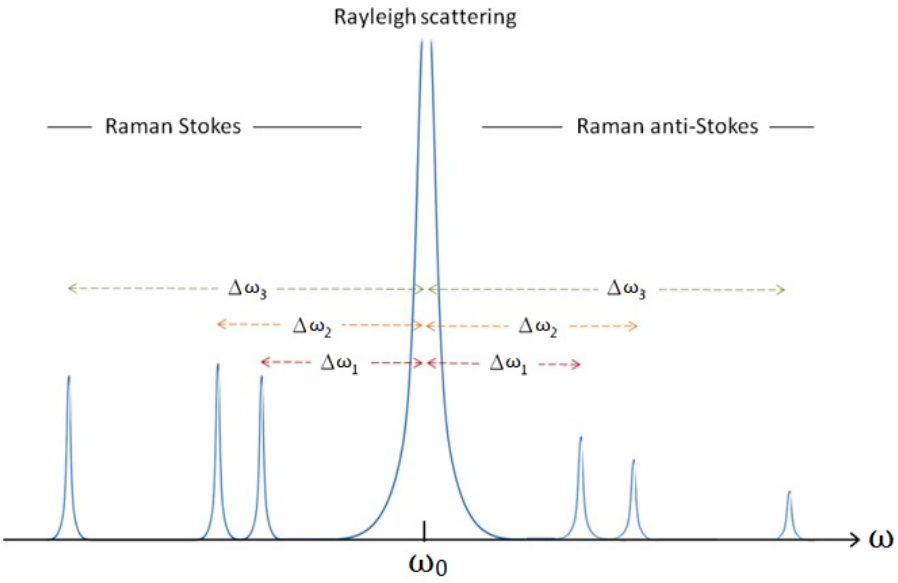

Figure 4 – **The Raman scattering draft**. From left to right: the Stokes, Rayleigh and anti-Stokes peaks are represented. $\Delta\omega_1, \Delta\omega_2$ and $\Delta\omega_3$ are the frequencies of three distinct vibrations, where $\Delta\omega_i = |\omega_i - \omega_0|$. The intensity differences between the Stokes and Anti-Stokes scatterings can only be explained by the quantum formalism, which will be described in the next section. Taken and adapted from reference [35].

The intensity of the Raman scattered light can be calculated by taking the time-averaged power radiated by the polarization $\mathbf{P}_{vib}$ [34]. In our Raman experiment, only the Stokes frequencies were collected. The intensity of the Stokes scattering depends on the polarization of the scattered radiation, $\hat{e}_s$, as $|\mathbf{P}_{ind} \cdot \hat{e}_s|^2$. By considering a polarization of the incident light $\hat{e}_i$, the intensity of the Stokes scattering, I_s, can be written as:

$$I_s \propto \left| \hat{e}_i \cdot \left(\frac{\partial \overleftrightarrow{\chi}}{\partial \mathbf{Q}^k} \right)_0 \mathbf{Q}^k(\omega) \cdot \hat{e}_s \right|^2 \tag{2.9}$$

At this point, a couple of remarks should be discussed. First, even if there is a atomic vibration, it is possible that there is no scattering if the electric susceptibility tensor does not vary with it, i.e. $\left(\frac{\partial \overleftrightarrow{\chi}}{\partial \mathbf{Q}^k}\right)_0 = 0$. Second, since the electric susceptibility tensor can have complex elements when the material absorbs the incident light,its derivative can also have complex elements. Taking these remarks into account, we can define the Raman Tensor for a specific vibration k, $\overleftrightarrow{R}^k$ as,

$$\overleftrightarrow{R}^k = \left(\frac{\partial \overleftrightarrow{\chi}}{\partial \mathbf{Q}^k} \right)_0 \mathbf{Q}^k(\omega), \tag{2.10}$$

where $\overleftrightarrow{R}^k$ is a second rank tensor with complex elements. Indeed, Raman tensor with complex elements has been reported for different materials [36–39].

Hence, the expression for the Raman efficiency can be re-written as,

$$I_s^k \propto |\hat{e}_i \cdot \overleftrightarrow{R}^k \cdot \hat{e}_s|^2. \tag{2.11}$$

In expression (2.11), neither $\hat{e}_i \cdot \overleftrightarrow{R}^k$ or $\overleftrightarrow{R}^k \cdot \hat{e}_s$ can be a null vector. As aforementioned, the Raman tensor can have complex elements, but it can be discussed in more details since the Raman Tensor is closely related to electric susceptibility. For instance, for non-magnetic materials (which is the $ReSe_2$ case) the electric susceptibility is a symmetric tensor [40, 41]. Moreover, the zero components can be obtained by group theoretical methods, where the symmetry of the crystal and symmetry of the vibrational modes are considered [42].

Therefore, by these arguments, it can be shown that the Raman Tensor for the vibrational modes of the $ReSe_2$, which belongs to the A_g irreducible representation of the C_i point group, can be written as,

$$\overleftrightarrow{R}^k = \begin{pmatrix} u & v & a \\ v & w & b \\ a & b & c \end{pmatrix}, \text{ where } \quad u, v, w, a, b, c \in \mathbb{C}. \tag{2.12}$$

Since, in our experimental setup, only the back-scattered light is collected and we are just interested in the projection of the Raman Tensor in the $xy-$plane of the laboratory frame, we will then consider only the following block of the Raman Tensor:

$$\overleftrightarrow{R}^k_{xy} = \begin{pmatrix} u & v \\ v & w \end{pmatrix}, \text{ where } \quad u, v, w \in \mathbb{C}. \tag{2.13}$$

The classical formalism discussed in this section not only presents a reasonable description of the Raman effect origin but also leads to an important result for the scattering intensity, expression (2.11). Equation (2.11) contains all the information of the angular dependence of the Raman response of a lattice vibration. Accordingly, this formalism will be extensively used in our work to investigate the anisotropic behavior of $ReSe_2$'s vibrational modes.

Nevertheless, such formalism does not explicit the dependence of the Raman effect with the wavelength of the incoming light beam and its interaction in the atomic level. Then, for completeness, in the next section, we will examine the quantum description for the Raman effect.

2.2 The microscopic treatment

The classical theory of the Raman scattering previously discussed, presents a reasonable well-description of the Raman (Stokes or anti-Stokes) scattering intensity as a function of the polarization of the incident and scattered lights (equation (2.11)). The classical theory also provides a satisfactory explanation for the origin of the Raman scattering. However, it fails to explain some features of the Raman effect. For instance, why is the intensity of Stokes scattering usually higher than the anti-Stokes intensity? (see Figure 4). The elucidation of this point, as well as for many other unmentioned here, was formally ascribed in a quantum approach in 1963 by Rodney Loudon [43].

Before we start, let us first specify the states that characterize a system composed of electrons and phonons that participate in the scattering of both the incident and scattered light in a crystal. Before the scattering, the system is in an initial state $|i\rangle = |N_i, N_s, N_q, \varphi_0\rangle$ comprising N_i photons of frequency ω_i, N_s photons of frequency ω_s, N_q phonons of wavevector q and no excited electron, i.e. the electron is in the fundamental state, denoted φ_0.

The Hamiltonian of this system can be written as,

$$\mathcal{H} = \mathcal{H}_0 + \mathcal{H}_1, \tag{2.14}$$

Here, $\mathcal{H}_0$ is the unperturbed Hamiltonian and given by, $\mathcal{H}_0 = \mathcal{H}_e + \mathcal{H}_L + \mathcal{H}_R$, where $\mathcal{H}_e$, $\mathcal{H}_L$ and $\mathcal{H}_R$ are the electron, lattice and radiation Hamiltonians, respectively. $\mathcal{H}_1$ is the Hamiltonian of the perturbation and written as, $\mathcal{H}_1 = \mathcal{H}_{eL} + \mathcal{H}_{eR}$, where $\mathcal{H}_{eL}$ and $\mathcal{H}_{eR}$ are, respectively, the electron-lattice interaction and electron-radiation interaction Hamiltonians.

One of the possible scattering processes can be described as follows: an electron at the initial state $|i\rangle$ absorbs an incoming photon of energy $E_i = \hbar\omega_i$ and creates an electron-hole pair sending the system to an intermediate state $|a\rangle$ via the electron-radiation interaction, $\mathcal{H}_{eR}$. Thus, the electron or the hole pair is scattered via the electron-phonon interaction, $\mathcal{H}_{eL}$, emits a phonon of energy $E_{ph} = \hbar\omega_{ph}$ and, then the system goes to another intermediate state $|b\rangle$. Finally, the electron-hole pair recombines via $\mathcal{H}_{eR}$, i.e. the electron goes back to its initial state with an emission of a new photon with energy $E_s = \hbar\omega_s$. Then, the system goes to the final state $|f\rangle$ [34]. This scattering process evolution can be represented in the Feynman diagram, as shown in Figure 5.

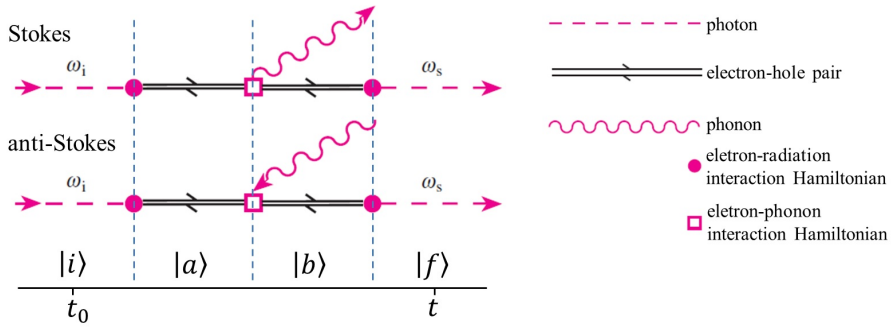

Figure 5 – **Feynman diagrams for one-phonon Stokes and anti-Stokes scattering.** (Left-side) Time evolution of the states of a system for one-phonon Stokes and anti-Stokes scattering from t_0 to t. The curly arrow pointing towards in or out the square vertex represents the annihilation or creation of a phonon, respectively. (Right-side) Explanation of the symbols used in the drawing Feynman diagrams to represent the Raman scattering. Taken and adapted from reference [22].

The states and energies of the process described above can be written as,

$$\begin{aligned}
|i\rangle &= |N_i, N_s, N_q, \varphi_0\rangle, \;\; E_i = N_i\hbar\omega_i + N_s\hbar\omega_s + N_q\hbar\omega_q + E_e^{\nu} \\
|a\rangle &= |N_i - 1, N_s, N_q, \varphi_e^c\rangle, \;\; E_a = (N_i - 1)\hbar\omega_i + N_s\hbar\omega_s + N_q\hbar\omega_q + E_e^{c} \\
|b\rangle &= |N_i - 1, N_s, N_q \pm 1, \varphi_e^c\rangle, \;\; E_b = (N_i - 1)\hbar\omega_i + N_s\hbar\omega_s + (N_q \pm 1)\hbar\omega_q + E_e^{c} \\
|f\rangle &= |N_i - 1, N_s + 1, N_q \pm 1, \varphi_0\rangle, \;\; E_f = (N_i - 1)\hbar\omega_i + (N_s + 1)\hbar\omega_s + (N_q \pm 1)\hbar\omega_q + E_e^{\nu}
\end{aligned} \tag{2.15}$$

where E_e^{ν} and E_e^{c} are, respectively, the energies of the electron in the valence and conduction bands. N_q+1 and N_q-1 correspond to the number of phonons in the Stokes and anti-Stokes scattering, respectively.

The efficiency of the Stokes (or anti-Stokes) scattering process can be calculated using third order perturbation theory according to [44]:

$$I \propto \frac{d}{dt}\left|\langle f|e^{-\frac{i\mathcal{H}(t-t_0)}{\hbar}}|i\rangle\right|^2 \tag{2.16}$$

Equation (2.16) gives the probability transition rate of a system going from a initial state $|i\rangle$ with energy E_i to a final state $|f\rangle$ with energy E_f and density of states $\rho(E_f)$.

Thus, it can be shown that the probability $\mathcal{P}_{Stokes}$ of the Stokes scattering, for a

phonon with energy $\hbar\omega_q$, derived from (2.16) is given by [34]

$$\mathcal{P}_{Stokes} = \left(\frac{2\pi}{\hbar}\right)\left|\sum_{a,b}\frac{\langle f|\mathcal{H}_{eR}|b\rangle\langle b|\mathcal{H}_{eL}|a\rangle\langle a|\mathcal{H}_{eR}|i\rangle}{[\hbar\omega_i-(E_a-E_i)][\hbar\omega_i-\hbar\omega_q-(E_b-E_f)]}\right|^2\times\delta(\hbar\omega_i-\hbar\omega_q-\hbar\omega_s) \tag{2.17}$$

or even,

$$\mathcal{P}_{Stokes} = A\left|\sum_{a,b}\frac{\langle f|\mathcal{H}_{eR}|b\rangle\langle b|\mathcal{H}_{eL}|a\rangle\langle a|\mathcal{H}_{eR}|i\rangle}{[\hbar\omega_i-(E_a-E_i)][\hbar\omega_i-\hbar\omega_q-(E_b-E_f)]}\right|^2 \tag{2.18}$$

where, according to (2.15), $E_i = E_f = E_e^\nu$, $E_a = E_b = E_e^c$ and A is a constant. Consequently, $E_a - E_i = E_b - E_f = E_e^c - E_e^\nu = E_g$, with E_g defined as the band gap energy of the crystal. Two resonance conditions can be achieved in (2.18): *i*. one occurs when $\hbar\omega_i = E_g$, i.e. the energy of the incident photon coincides with the band gap energy of the semiconductor; *ii*. the other occurs when $\hbar\omega_i = E_g + \hbar\omega_q$, i.e. the energy of the incoming photon is equal to the band gap energy of the semiconductor plus the energy of the created phonon.

When either one of these resonances occurs, the denominator of (2.18) vanishes leading to an unphysical situation. To avoid that, it is necessary to consider that the intermediate states $|a\rangle$ and $|b\rangle$ have finite lifetimes, τ_a and τ_b, respectively, and for that reason, damping constants $i\Gamma_a = i\hbar/\tau_a$ and $i\Gamma_b = i\hbar/\tau_b$ are added to the energies E_a and E_b, i.e. $E_a \to E_a + i\Gamma_a$ and $E_b \to E_b + i\Gamma_b$. Therefore, (2.18) can be re-written as

$$\mathcal{P}_{Stokes} = A\left|\sum_{a,b}\frac{\langle f|\mathcal{H}_{eR}|b\rangle\langle b|\mathcal{H}_{eL}|a\rangle\langle a|\mathcal{H}_{eR}|i\rangle}{[\hbar\omega_i-E_g+i\Gamma_a][\hbar\omega_i-(\hbar\omega_q+E_g)+i\Gamma_b]}\right|^2 \tag{2.19}$$

To this end, we stress some comments before proceed to the next section. The process described above contains an implicit assumption that must be unveiled: the need of the participation of the electron in the process. In other words, why is the light not directly scattered by the phonon? The explanation of this issue comes from the fact that the photon-phonon interaction is very weak when the frequency of the phonon is not comparable to that of the incoming photon. Therefore, from the near-infrared to higher frequencies, that term is negligible and the main process responsible for the scattering is the electron mediation [34]. The last remark consists in the fact the there are five other processes contributing to the Stokes scattering and a better description of them can be found in [34].

2.3 Raman Spectroscopy on Re-based TMDs

In this section, we review the state-of-art of Raman spectroscopy on rhenium dichalcogenides (e.g., $ReSe_2$ and ReS_2). There are more works on ReS_2 than on $ReSe_2$ but

similar behaviour are expected for both of them since they have analogous crystal structure. The first study of Raman Spectroscopy in $ReSe_2$ was reported by Wolverson *et al.* [26]. The authors have performed group theory analysis to predict all the Raman active modes of $ReSe_2$ and their irreducible representations (see section 1.2). In the same work, it was also calculated the frequency positions of the 18 predicted modes by Density Functional Perturbation theory (DFPT). The results were then compared to the 16 experimentally observed modes, as shown in Table 1. It was also reported polarized Raman measurements, where the authors used a linearly polarized incident laser and an unpolarized detection to study the angular dependence of the $ReSe_2$ modes, see Figure 6(a) [26]. Moreover, according to Wolverson *et al.* it is possible to determine the crystallographic orientation of the samples from those polarized Raman spectra [26]. In the latter case, it was assumed that the Raman tensor has only real elements [26] and the Raman intensity (which can be derived from equation (2.11)) as a function of the angle, θ – angle of the incident light and the "x" axis of laboratory frame – was written as [26],

$$I_s \propto u^2 \cos^2(\theta) + w^2 \sin^2(\theta) + v^2 + v(u+w)\sin(2\theta) \tag{2.20}$$

Table 1 – **First order modes of $ReSe_2$.** Calculated and observed frequencies of the 18 A_g modes of $ReSe_2$. Taken from reference [26].

Calculated (cm^{-1})	Observed (cm^{-1})	Calculated (cm^{-1})	Observed (cm^{-1})
103.6	110.0	197.7	194.0
118.0	116.7	206.8	207.7
123.1	-	219.9	217.2
125.9	123.8	235.1	231.8
162.5	158.2	242.4	239.0
175.6	171.0	251.7	247.1
179.4	179.0	265.8	260.4
182.6	-	287.9	283.6
194.9	190.0	298.4	293.9

In 2015, Zhao *et al.* reported new outcomes of polarized Raman measurements: the low-frequency modes in monolayer, few-layers and bulk $ReSe_2$ [27], as shown in Figure 6(b). These low frequency modes appear bellow 50 cm^{-1} and are associated with the interlayer vibrations, known as shear (in-plane) and breathing (out-of-layer) modes. Note that the intensity and frequency position of these modes change as the number of layer increases and also that those modes are absent in the single-layer sample (see Figure 6(b)). Therefore, the analyses of the Raman spectrum of the low-frequency modes is a reliable method to identify the number of layers in $ReSe_2$ [27, 30].

Due to the anisotropic property of Re-based TMDs, polarized Raman experiments are essential to probe their phonon spectra. In both previous works [26, 27], the same

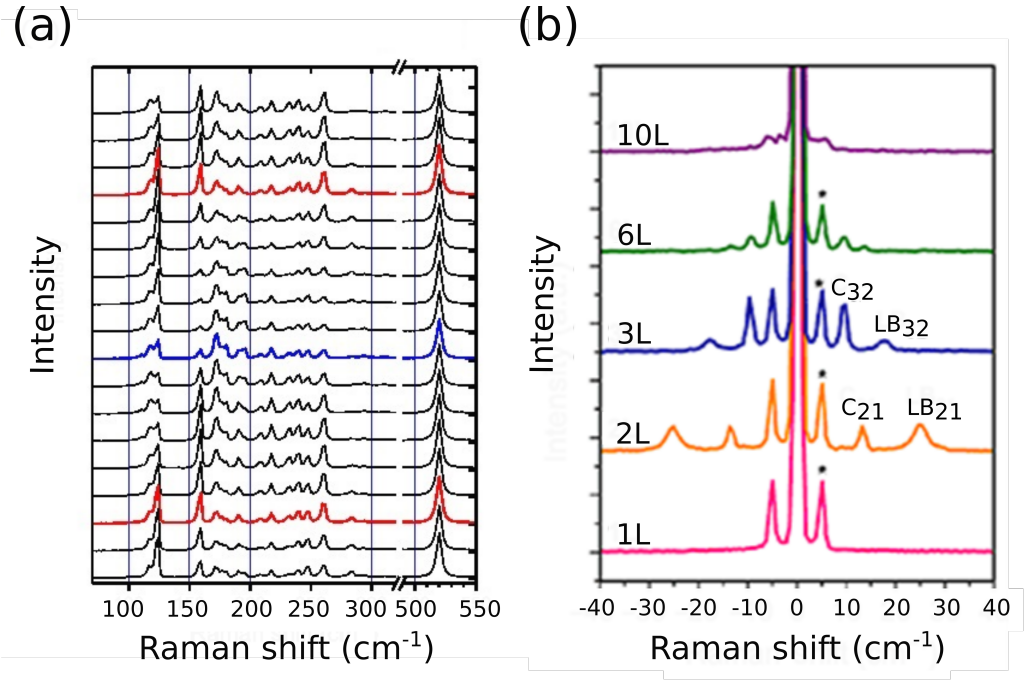

Figure 6 – **Polarized Raman on $ReSe_2$.** (a) Raman spectra of $ReSe_2$ as a function of the angle of rotation of the excitation polarization with 15° steps. The data were collected with an excitation wavelength of 532 nm. The zero of the angle scale is defined by the experimental setup, and thus it is arbitrary with respect to the crystallographic axes of the sample. The spectra are unnormalized. The red (0° and 180°) and blue (90°) spectra are highlighted to demonstrate that the same spectrum is obtained after rotation of the excitation polarization by 180°. (b) Raman spectra of the low-frequency modes, shear (C) and breathing (LB) modes, in $ReSe_2$ showing their intensity and frequency position evolution as the number of layers increase. The asterisks in (b) represent Brillouin scattering of silicon substrate. Taken and adapted from references [26, 27].

configuration for the polarized Raman experiments was used. However, Lorchat *et al.* have considered a different configuration setup to study the interlayer vibrations [30]. The $ReSe_2$ sample was rotated with respect to the linearly polarized light and an analyzer was placed before the entrance of the spectrometer to select the scattered light parallel or perpendicular to the polarization of the incoming laser photon. Such configuration provided considerable changes in the angular patterns of the integrated intensities of the inter- and intra-layer modes [30]. The angular pattern variation was analyzed considering the fact that the Raman tensor has complex elements [30].

Additionally, birefringence may also play an important, and qualitative, role on the Raman response of other anisotropic materials such as $\beta-Ga_2O_3$ and ReS_2 [45, 46]. For these materials, it is necessary to consider changes in the polarization of the incident and scattered electric fields by applying the Jones matrix $\mathbf{J}$ on the Raman tensor. It corresponds to transform the Raman tensor to an effective Raman tensor, $\mathcal{R}_{eff} = \mathbf{J}\mathcal{R}\mathbf{J}$. In this case, for an experiment performed in the back-scattering geometry, with a light of

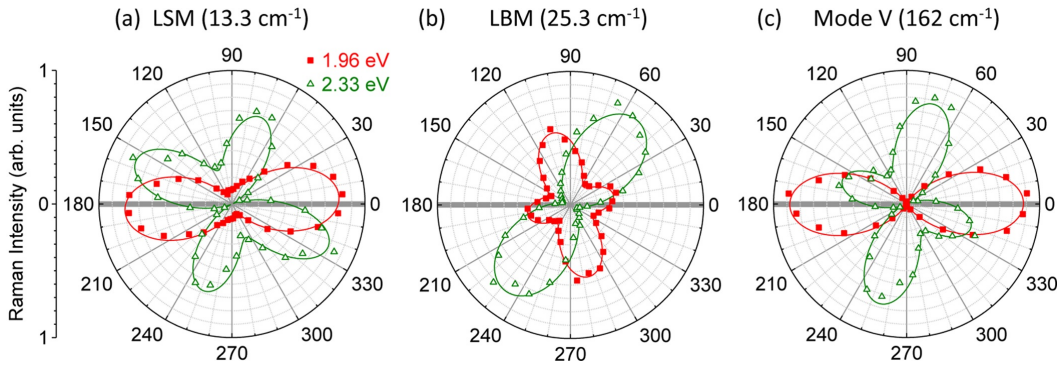

Figure 7 – **Polar plots of bilayer $ReSe_2$** modes. Polar plots of the integrated Raman intensity of (a) the low-frequency the shear mode (LSM), (b) low-frequency breathing mode (LBM) and (c) the fifth high-frequency mode that appear in the spectrum, named mode V, recorded as a function of the angle θ between the linearly polarized laser field and the Re chains (solid gray lines in (a−c)), at two different photon energies $E_L = 1.96$ eV (red squares) and $E_L = 2.33$ eV (open green triangles) in the parallel (XX) configuration. The angular patterns are normalized for a clearer comparison. The solid lines are fits to the experimental data considering a Raman tensor with complex elements. Taken and adapted from reference [30]

wavelength λ and a slab of thickness z, the Jones matrix is given by

$$\mathbf{J} = \begin{pmatrix} 1 & 0 \\ 0 & e^{i\chi(z)} \end{pmatrix} \tag{2.21}$$

where $\chi(z)$ is the phase shift between the light with polarization along the fast and slow axes, where Δn is the difference of the refractive indices, and can be written as $\chi(z) = \frac{2\pi\Delta n z}{\lambda}$ [46]. This effect was observed for ReS_2 [46] and it may also happen in $ReSe_2$.

An interesting and unusual feature of the Re-based TMDs is the existence of a vertical orientation ($+\overrightarrow{z}$ or $-\overrightarrow{z}$) due to the absence of a rotation axis in the layer plane, i.e. it is possible to distinguish if the crystal is flipped upside down with respect to other flake with the same thickness [47]. Thus, consider a rotation $\mathbf{T}$ by π through the x axis of the back-scattering geometry of the laboratory frame (recall that $\mathbf{T}$ is not a symmetry operation for the C_i point group). Applying this rotation to the Raman Tensor in equation (2.12), the transformed tensor $\mathcal{R}'$ will be $\mathcal{R}' = \mathbf{T}^{-1}\mathcal{R}\mathbf{T}$. Then,

$$\mathcal{R}' = \mathbf{T}^{-1}\mathcal{R}\mathbf{T} = \begin{pmatrix} 1 & 0 & 0 \\ 0 & -1 & 0 \\ 0 & 0 & -1 \end{pmatrix} \begin{pmatrix} u & v & a \\ v & w & b \\ a & b & c \end{pmatrix} \begin{pmatrix} 1 & 0 & 0 \\ 0 & -1 & 0 \\ 0 & 0 & -1 \end{pmatrix}$$

$$\mathcal{R}' = \begin{pmatrix} u & -v & -a \\ -v & w & b \\ -a & b & c \end{pmatrix} \tag{2.22}$$

Therefore, it can be seen that in the $xy-$plane the effect of this rotation is the change $v \to -v$ and it modifies the intensity in (2.20) to

$$I_s \propto u^2 \cos^2(\theta) + v^2 + w^2 \sin^2(\theta) - v(u+w)\sin(2\theta). \tag{2.23}$$

Since the last term of the equation (2.23) has opposite sign from equation (2.20), the vertical orientation should matter in the Raman response of the material. And, it indeed does [47]. Moreover, it has been reported the possibility to distinguish the vertical orientations of Re-based TMDs by Raman spectroscopy in two different ways. The first one consists by the comparison of the angular dependence orientation of the Raman modes in each structure, as shown in Figure 8 for ReS_2 [47]. This methodology has been reported in the literature for both $ReSe_2$ and ReS_2 [47].

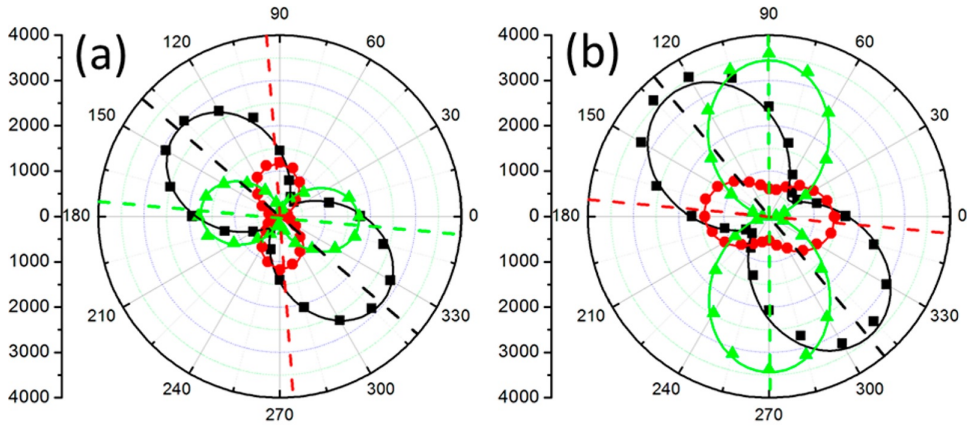

Figure 8 – **Polar plots of of bulk ReS_2.** Intensities as a function of angle with respect to the arbitrary laboratory x axis of three peaks in the Raman spectra of large ReS_2 flakes (both of thickness >100 nm) which were cleaved from the same starting crystal but were facing (a) "upward" and (b) "downward". The peaks chosen are the 150, 160, and 211 cm^{-1}, named as modes III−V, corresponding to black squares, red circles, and green triangles, respectively. The solid lines correspond the respective fits to the experimental data according to equation (2.20) and the dashed lines indicates the orientation of the principal axis obtained from each fit. A 532 nm excitation wavelength was used to record the spectra. Taken and adapted from reference [47].

In the second one, instead of collecting several Raman spectra, as the former method requires, we just need to record the spectra with left- and right-handed circularly polarized light, LCP and RCP, respectively, as shown in Figure 9), then we calculate the circular intensity differential (CID), Δ, which is defined as

$$\Delta = \frac{I^R - I^L}{I^R + I^L} \tag{2.24}$$

Here, I^R and I^L are the intensities of a mode collected in the right- and left-handed circularly polarized light configuration, respectively. The CID has opposite signs for

opposite vertical orientations, and it also depends on the mode selected and the thickness of the sample [46]. The second methodology has only been reported for the ReS_2 case [46] and similar results are expected for $ReSe_2$.

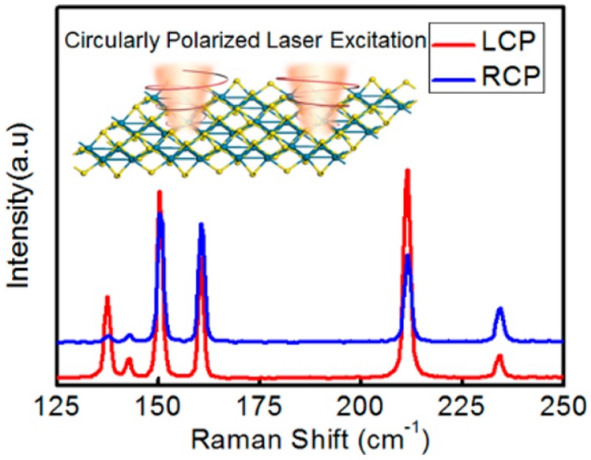

Figure 9 – **Circularly polarized Raman spectra of ReS_2.** Raman spectrum recorded in the left-handed (red color) and right-handed (blue color) circularly polarized light. The Raman spectrum was collected using a 514.5 nm laser wavelength. Taken and adapted from reference [46].

3 Experimental Methods

In this chapter, we present the experimental methodology used in this work. Basically, it consists of three steps: sample preparation, characterization and polarized Raman measurements. We start describing the method used to obtain the $ReSe_2$ samples followed by the features of our Raman instrumentation and by details of the measuring procedures.

3.1 Sample preparation

Literature reports show that $ReSe_2$ has been obtained by mechanical exfoliation [26, 27, 30, 47] and chemical vapor deposition [48–50] methods. In our work, we opted to use the mechanical exfoliation (also known as "Scotch tape method" or "micro-mechanical cleavage") which is the most used technique for obtaining 2D layered materials due to its simplicity and sample quality [5]. This method was developed by Novoselov and Geim who shared the Nobel Prized in 2010 for groundbreaking experiments regarding the two-dimensional material graphene [3, 10, 51].

Figure 10 shows the exfoliation procedure of a 2D layered material as illustrated by Yi *et al.* work [52]. First, a piece of bulk crystal of a layered material is placed on a Scotch tape, then folded it. By doing that, there will be one piece of the bulk crystal on each side thinner than the original one. This step is repeated several times in order to decrease thickness of the crystal. Finally, the tape is sticked onto a desired substrate, usually a Si/SiO_2 substrate, then it is slowly removed. This last step is the "final exfoliation" that will reduce even more the thickness of the crystals in the tape by leaving many of them on the substrate [10].

The last two frames of Figure 10 shows our $ReSe_2$ exfoliated sample which was produced in the Clean Room of the Physics Department of Federal University of Minas Gerais by Juliana Brant and Jessica Santos Lemos and studied in this work. The $ReSe_2$ crystal used in the exfoliation was obtained from a collaboration with Terrones's group from Pennsylvania State University.

Typically, though it is not always true, the long edge of the sample can be recognized as being parallel to the rhenium chains [47], as shown in Figure 3(d). For our obtained sample, we have assumed that this was the case since the single-layer is attached to a large bulk. We have also considered the direction of the rhenium chains to be parallel to the $b-$axis instead of the $a-$axis, an approach used by Hart *et al.* [47], as shown in Figure 3.

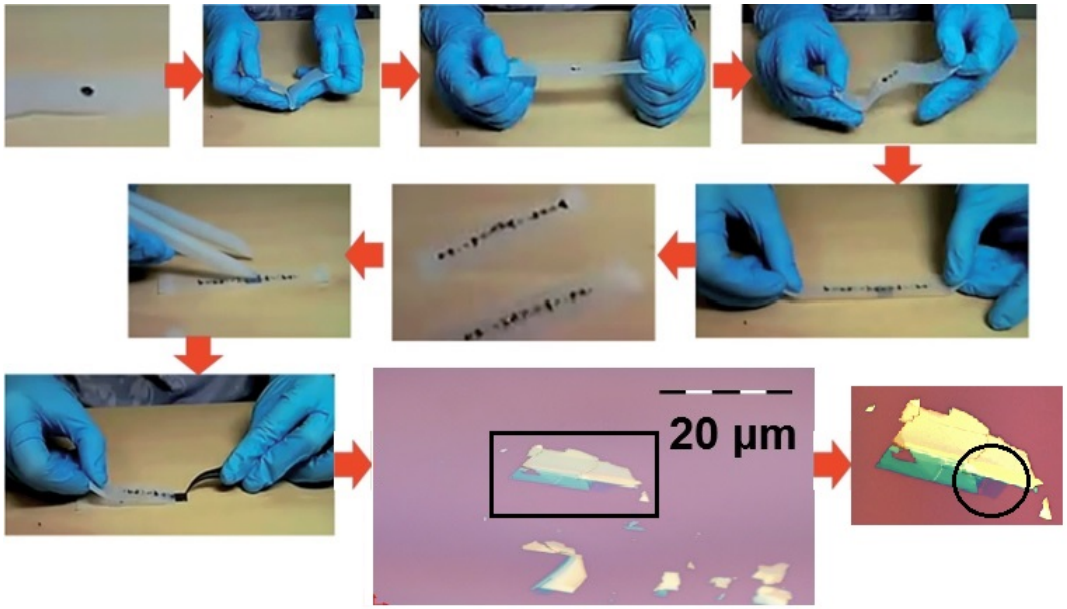

Figure 10 – **Micro-mechanical cleavage method.** Exfoliation steps of the mechanical cleavage used to obtain single- and few-layers of two-dimensional materials. The single-layer $ReSe_2$ sample used in this work is shown in the last two frames, while the procedure was taken from reference [52].

3.2 Sample characterization

After the sample preparation one needs to find a way to identify the number of layers. There are many techniques that can be used to achieve such goal: contrast in the optical image [53], atomic force microscopy [26, 27], photoluminescence spectroscopy [27], Raman spectroscopy [27,30] and others. Among all of these techniques Raman spectroscopy has proven to be the versatile tool to characterize 2D materials since it is a non-invasive and non-destructive technique that allows to identify several features in 2D materials [54]. For instance, it has been reported in graphene and semiconducting TMDs that Raman spectroscopy allows us to probe the number of layers [55, 56], strain [55, 56], isotope [57], doping [58] and defects [55, 59].

In semiconducting TMDs (e.g. MoS_2, WS_2), the identification of the number of layers is given by the frequency difference of the A_{1g} (out-of-plane) and E^1_{2g} (in-plane) modes [19], as well as the measurement of the low-frequency modes [60]. In the $ReSe_2$ (and ReS_2) case, not only the number of layers can be identified [26, 27] but also the $z-$axis direction of the sample [47]. According to refs. [27,30], the number of layer in $ReSe_2$ can be characterized by tracking the low-frequency modes of the material. It was reported that the absence of the shear and breathing mode is the fingerprint of a single-layer sample [27, 30]. To do so, one also needs to consider the substrate response at the low-frequency range. Figure 11(a) shows the low-frequency Raman spectra of the silicon substrate and single- (1L), bi- (2L) and tri-layer (3L) $ReSe_2$ of our own production, recorded with a 2.33 eV

excitation energy. Notice that the presence (or absence, the single-layer case) of the interlayer modes are in agreement with the results reported by Lorchat *et al.* [30], as shown in Figure 11(b). The sample identified as single-layer $ReSe_2$, shown in Figure 10, is the one used in our study.

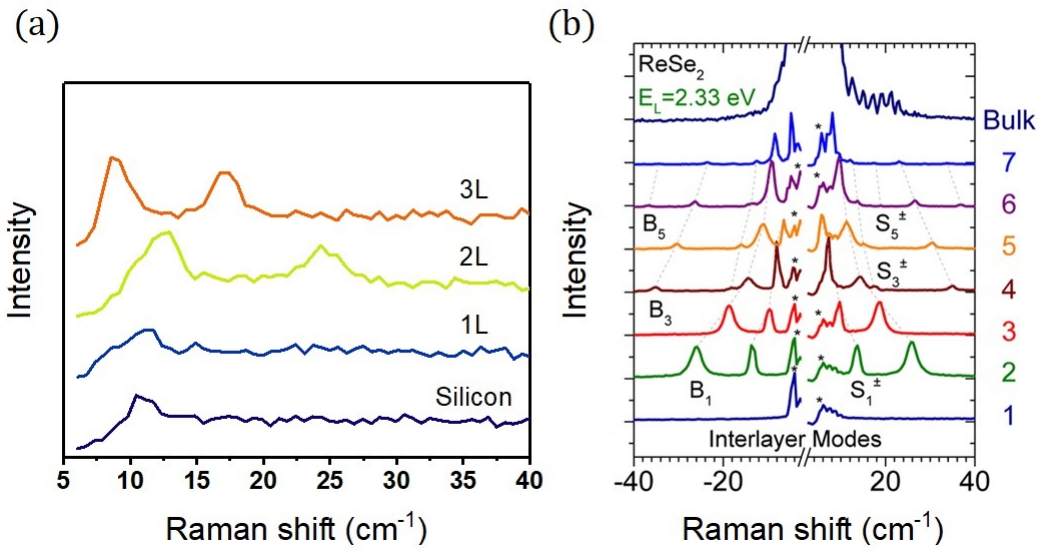

Figure 11 – **Low-frequency modes of $ReSe_2$.** (a) Raman spectra of the silicon substrate and of the 1L, 2L and 3L $ReSe_2$ samples, of our own production. The Raman spectra were collected using a 2.33 eV laser energy. The results are in accordance with the assignments of layer number of ref. [30] shown in (b). "B's" correspond to the breathing modes while "S's" correspond to the shear modes. Taken and adapted from reference [30].

As aforementioned, Re-based TMDs possess two possible vertical orientations ($+\overrightarrow{z}$ or $-\overrightarrow{z}$) [47]. However, we were not able to distinguish the orientation of the $z-$axis of our single-layer sample as performed in ref. [47], due to the following two reasons: (i) there is no report in the study of the vertical orientation for the monolayer regime; only for bulk [47]. (ii) thus far, we were able to obtain only one single-layer sample to perform the Raman measurements proposed in this Master thesis. Nevertheless, since there is no possible ambiguity between the effects of the in-plane and vertical orientations in the study of the angle-dependence of polarized Raman spectra [47], a correction of the orientation distinction of our single-layer sample can be performed in the future.

3.3 Instrumentation

The Raman measurements presented in this Master thesis were recorded in a *Horiba Jobin Yvon T64000* spectrometer. This system has three possible configurations, as shown in Figure 12. It consists of one monochromator, used in the single and triple monochromator modes; and two monochromators, that are used in triple-additive and

triple-subtractive modes. The set formed by the first two monochromators is named as pre-monochromators, whereas the last one is called spectrograph. Each monochromator is composed by a holographic diffraction grating and two concave mirrors.

The single-monochromator mode has the shortest optical path among these configurations since the light does not pass through the pre-monochromators. In other words, the light goes directly to the spectrograph and, for this reason, it also has the best signal/noise ratio. However, it needs special filters (edge or notch filter) to block the Rayleigh scattering signal of each excitation wavelength. In addition, edge filters usually has cut widths higher than 100 cm^{-1} which precludes us to measure the interlayer modes.

The triple-additive mode has the best resolution since both three diffraction gratings work in series such that as light pass through the gratings it is highly dispersed. The disadvantage of this triple-mode is the lowest signal among the three configurations.

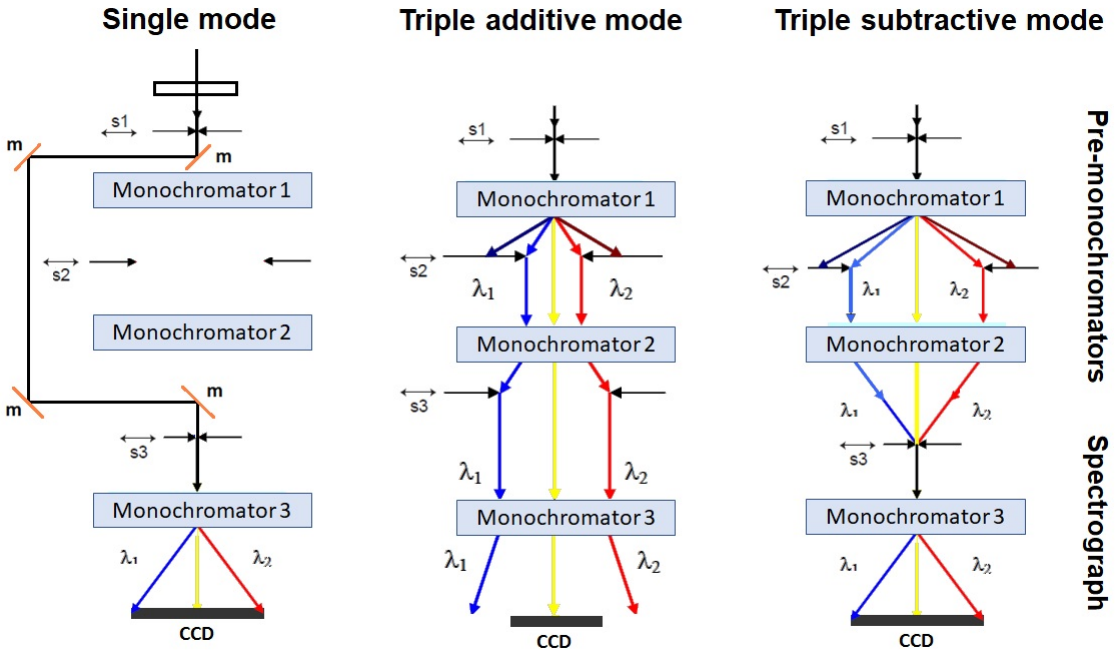

Figure 12 – **Configurations of the spectrometer.** In the single mode, the light goes directly to the spectrograph through successive reflections on the mirrors, "m". In the triple additive mode, all the slits (s1, s2 and s3) are open while the monochromators are working in series. In the triple subtractive mode, the first monochromator disperses the light, whereas the second one converges the light that pass through slits "s2" and slit "s3" and then it is dispersed again by the spectrograph. Taken and adapted from reference [61].

Therefore, we opted to use the triple-subtractive mode to perform our Raman measurements. In this set up, the pre-monochromators are used to get rid of the Rayleigh scattering while the third one is used to disperse light before it hits the detector. The main advantage of the triple-subtractive mode is the recording of the Raman spectrum in the desirable range of frequency for characterization (e.g. $< 50 cm^{-1}$). Also, there is no

need the use of edge or notch filters. This mode also works as an analyzer, blocking most of the light that comes with polarization in a determined direction.

In our work, we have used a 530.8 nm (2.34 eV) excitation wavelength from a Innova 70C Argon-Krypton laser source. An interference filter specific for this wavelength was used in order to cut-off the plasma lines from the laser source. The light emitted by the laser source is linearly polarized such that the direction of its polarization is aligned with the axis of the analyzer of the triple-mode described in the last paragraph. In the Polarized Raman context, we say that the measurements performed are in the "parallel configuration". Moreover, we also used a half-wave plate to rotate the incident beam by an angle of 90 degrees, thus having a "crossed (or perpendicular) configuration".

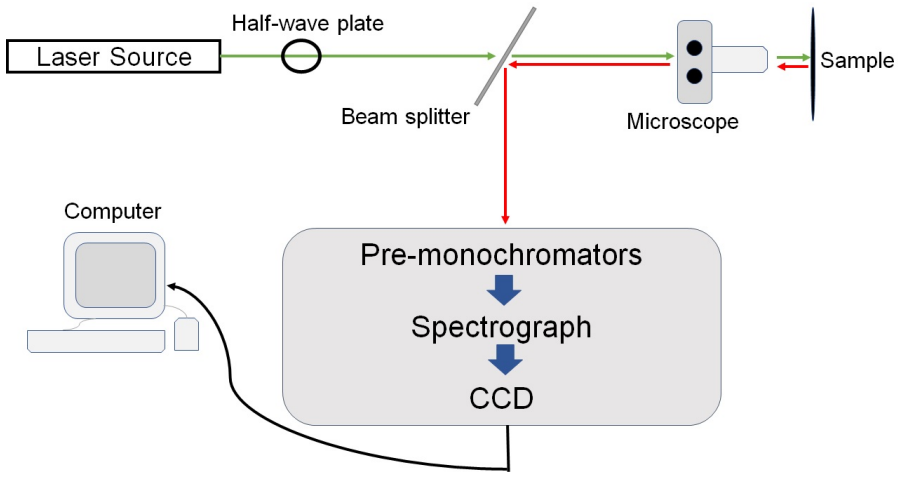

Figure 13 – **Experimental set up of our Raman laboratory.** The light is emitted by an Argon-Krypton laser source, then its polarization is rotated 90 degrees (or not) when it passes through a half-wave plate. Next, it is focused on the sample by the same lens that will collect the scattered light and sent to the detection system composed by three monochromators and analyzed in the computer. Author's own work.

The incident light was focused onto the sample using a 100× long work distance Olympus objective lens with 0.9 numerical aperture (N.A.), which also collects the scattered light in the back-scattering geometry of our system. In order to performed the polarized Raman measurements, the sample was placed on a goniometer and, then rotated by 10 degrees steps to each spectrum acquired. The polarized Raman spectra were collected from 0 to 360 degrees in both "parallel" and "crossed" configurations according to the descriptions above.

The illuminated area of the sample has a minimum diameter given by $d = \lambda\sqrt{\frac{1}{(N.A.)^2} - 1}$, considering a Gaussian shaped laser beam. Thus, for the laser source and objective used in our experiments, the minimum illuminated diameter onto the sample is approximately 257 nm, which is of the same order of magnitude of the excitation wavelength. Although, the diffraction limit permits laser beams of diameters similar or

even smaller than that, a real experiment has a spot size diameter in the order of 1 μm, which is the real spatial resolution of our system.

The collected inelastically scattered light is directed to a charge cooled device (CCD). The computer controls the gratings' movement associates each CCD column of pixels to a wavenumber. Then, it collects the results of all columns together to build the Raman spectrum by taking into account the amount of light each column received. Therefore, the spectral resolution of the spectrometer is related to how much the light can be dispersed before it reaches the detector. One of the ways to do that, is to enlarge the optical path from the spectrograph to the CCD, but such procedure decreases the signal intensity. An alternative way is to choose diffraction gratings of larger number of grooves per millimeter. For our system, we have used a 1800 grooves/mm diffraction grating with spectral resolution in the order of 1 cm^{-1}, which is satisfactory for our purposes. Figure 13 shows the schematic representation of our experimental set up described above.

4 Results and Discussion

In this chapter, we report the anisotropic response of single-layer $ReSe_2$ by polarized Raman spectroscopy. All the experimental data were collected in our Raman Laboratory at Federal University of Minas Gerais (UFMG - acronym in Portuguese). The sample used in this work as well as its production are described in the previous chapter. The results presented next are not published yet.

4.1 Raman-active modes

We start by probing the 18 A_g non-degenerate first-order modes predicted by group theory analysis (see section 1.2). Due to the low symmetry of $ReSe_2$, we need to be aware of the implications of Equation (2.11). Conventionally, the incoming laser beam is linearly polarized, i.e. $\hat{e}_i = (\cos(\theta), \sin(\theta), 0)$, where θ is the angle between the direction of light polarization and the $x-$axis of the laboratory frame which coincides with the $b-$axis of the crystal when $\theta = 0$. Thus, our concerns are directed to the scattered light collected by the detection system. If the detection is unpolarized from 100 to 300 cm^{-1} wavenumbers, shifted from the wavelength of excitation, we observe that the Raman efficiency for a $ReSe_2$ mode, considering only real elements in the Raman tensor, is given by (2.20):

$$I_s \propto u^2 \cos^2(\theta) + w^2 \sin^2(\theta) + v^2 + v(u+w)\sin(2\theta)$$

From the expression above, it can be seen that either the intensity vanishes for a specific θ_0, i.e. $I_s(\theta_0) = 0$, or it never vanishes no matter the direction in which the measurement is taken, i.e. $I_s(\theta) \neq 0$ for all θ. One should pay attention to the first case, since a Raman mode may not be observed in the collected Raman spectrum if the same was acquired in a direction θ_0 to which its intensity vanishes. This issue can be easily overcome by collecting the Raman spectrum in a different direction, i.e. rotating the sample or the incident light. It is noteworthy that since Equation (2.20) is a continuous function, small changes in the direction about that θ_0 may not be significant enough to turn the experimentally measurable intensities.

Figure 14 shows the Raman spectrum of a single-layer $ReSe_2$ for an excitation energy of 2.33 eV in the 100–300 cm^{-1} spectral range from our exfoliated sample. This Raman spectrum was collected with polarization of both incident and scattered light aligned to the assumed $b-axis$ (long edge of the sample, see Figure 10). The experimental Raman spectrum (blue dots) was fitted using a set of Lorentzian functions (orange curves)

to track the frequency position of each Raman mode. A zoom-in of three different regions is shown in the second row of the figure to clearly depict each Raman mode.

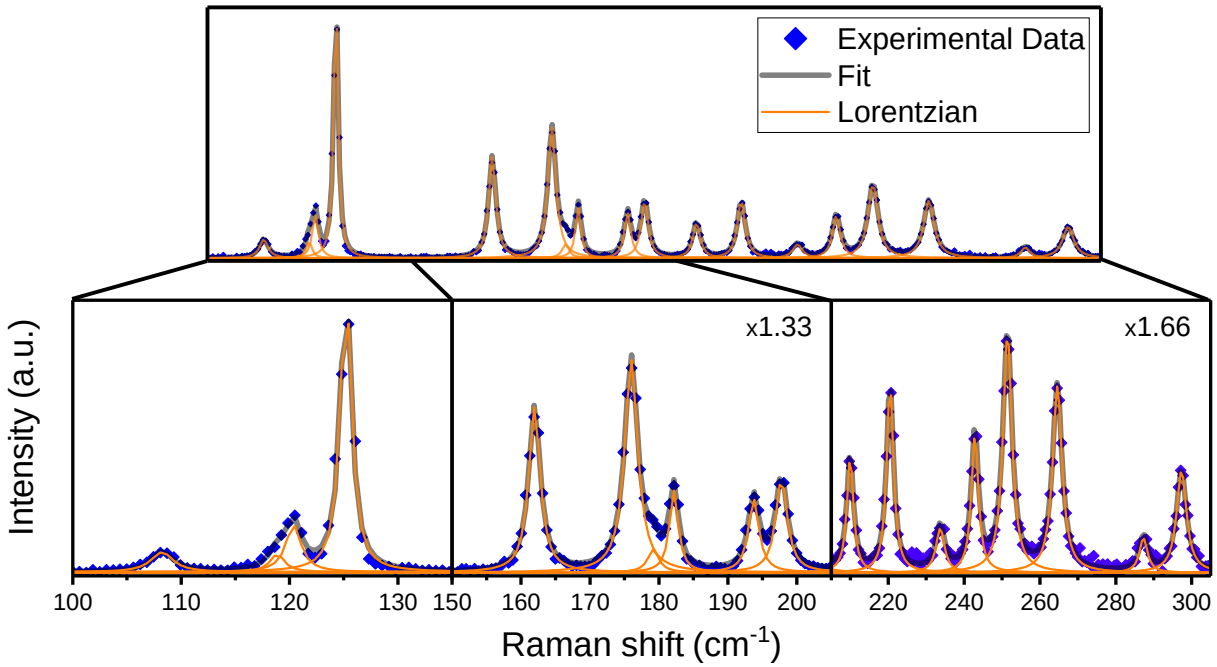

Figure 14 – **Raman spectrum of single-layer $ReSe_2$.** Top: overall Raman spectrum recorded with a 2.33 eV excitation energy in the parallel configuration (XX configuration). Bottom: Three regions of the spectrum are shown, from left to right, with no vertical zoom, with ×1.33 and with ×1.66 vertical zoom-in. Blue dots correspond to the experimental Rama spectrum and orange curves correspond to the Lorentzian function used to fit each peak. Author's own work.

In Fig. 14, all the 18 Raman modes predicted by group theory are observed where the lower (higher) frequency mode appears at 107.9 cm^{-1} (297.1 cm^{-1}). Table 2 shows the calculated and measured frequencies from Ref. [26] the observed frequencies of the Raman modes in our work, extracted from the fitting process shown in Fig. 14. The frequencies were calibrated by the silicon peak at 521.6 cm^{-1}, where one decimal place is kept because the fit error is 0.1 cm^{-1}. The measured frequencies of our work are in good agreement with the theoretical results from ref. [26]. Additionally, the two missing modes in ref. [26] can be seen at 118.6 cm^{-1} and 178.9 cm^{-1} in our measured Raman spectrum. We pointed out that the peaks at 118.6 cm^{-1} and 120.1 cm^{-1} are very close and near to the limit of our spectral resolution. On the other hand, the mode at 178.9 cm^{-1} is far enough from the adjacent peaks and can be better observed in other orientations (see below). Therefore, based on our Raman results, we have discarded the hypothesis that these two peaks were not previously observed in previous reports due to their Raman intensity were considerably low. Then, we conclude that the lack of observation of those mode in [26] is due to spectral resolution issues, since we used the same excitation energy of that work.

Table 2 – **First-order modes of $ReSe_2$.** Comparison of the calculated and measured frequencies of the 18 A_g Raman-active modes of $ReSe_2$. Taken from reference [26] and adapted with author's own work.

Calculated ref. [26] (cm^{-1})	From ref. [26] (cm^{-1})	Our work (cm^{-1})
103.6	110.0	107.9
118.0	116.7	118.6
123.1	-	120.1
125.9	123.8	124.9
162.5	158.2	161.7
175.6	171.0	175.7
179.4	179.0	178.9
182.6	-	181.9
194.9	190.0	193.4
197.7	194.0	197.5
206.8	207.7	209.7
219.9	217.2	220.2
235.1	231.8	233.4
242.4	239.0	242.5
251.7	247.1	251.1
265.8	260.4	264.3
287.9	283.6	286.6
298.4	293.9	297.1

4.2 Polarized Raman Spectroscopy

The importance of the sample's orientation with respect to the polarization of the incident and scattered lights is strengthened when an analyzer is used to collect the Raman spectrum in a specific orientation. We have performed polarized Raman measurements in both parallel and crossed configurations using a 2.33 eV excitation energy. The sample was rotated from 0° to 360° with a step of 10 degrees in the counterclockwise direction after each spectrum acquisition, where 0° is the direction of the $b-$axis of the sample. The evolution of the polarized Raman spectra in both configurations (parallel and crossed) is shown Figure 15 (a) and (b). All Raman data, for both configurations, were collected using the same laser power and exposure time with optimized focus for each measurement. Since the Raman spectra in both parallel and crossed configuration were collected under the same experimental conditions (including the grating position), the spectra were not normalized, i.e., both charts in the Fig. 15(a) and (b) are in the same scale. Only a smooth baseline was subtracted from the presented spectra.

Notice that some Raman modes are more pronounced in one configuration than in the other. For instance, the most pronounced peak of the parallel configuration is located at 124.9 cm^{-1}, and its substantial intensity remains for all the angles of this configuration (see Fig. 15(a)). However, this peak almost vanishes for some angles in the crossed configuration (see Fig. 15(b)). Additionally, in the crossed configuration the overlapping of the modes

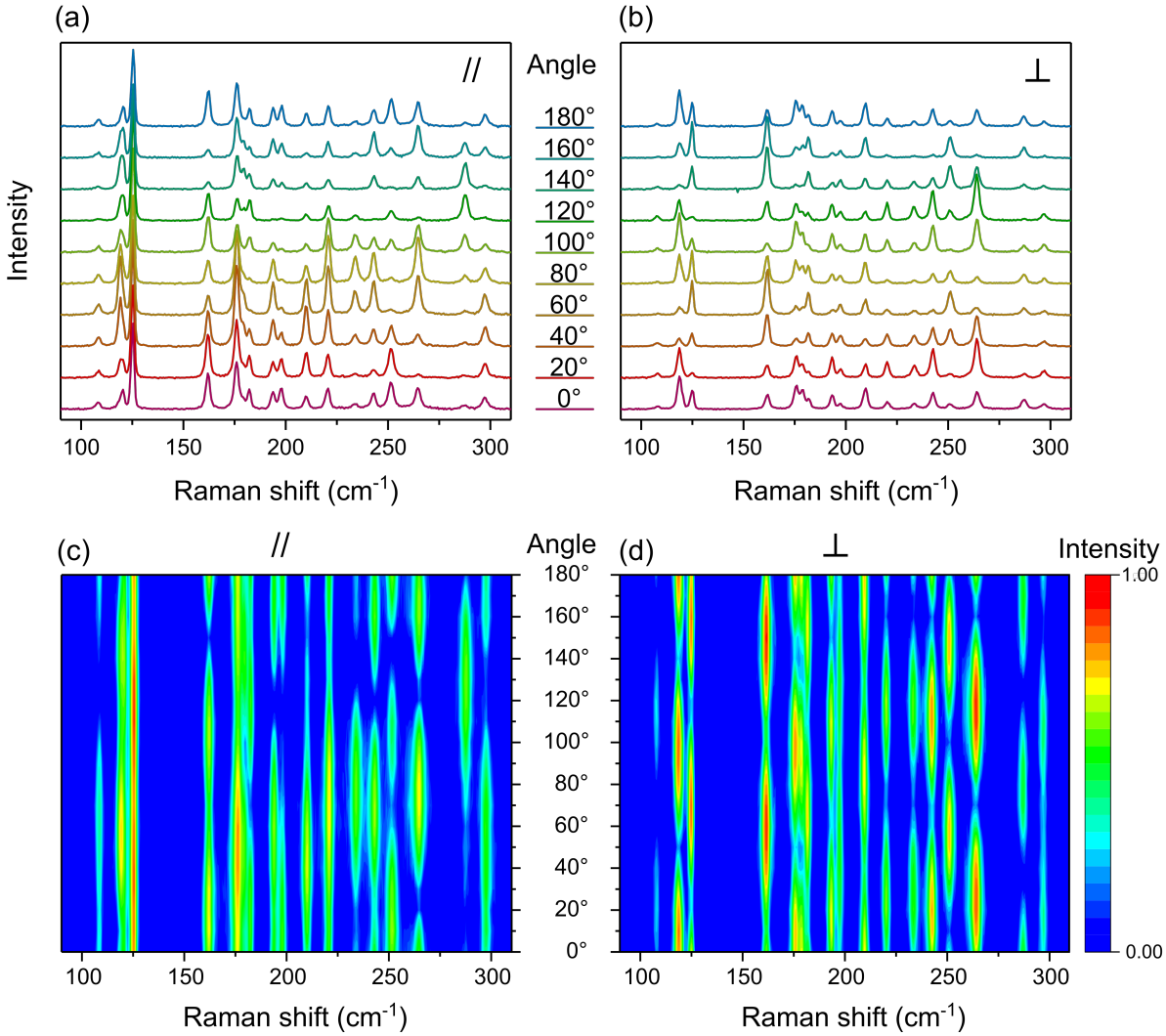

Figure 15 – **Polarized Raman spectra of a single-layer $ReSe_2$.** Raman spectra recorded in (a) parallel and (b) crossed configurations. The sample was rotated in steps of 10 degrees with respect to the fixed incident and scattered light polarizations. The zero degree corresponds to the alignment of the analyzer with the $b-$axis. Raman intensity map of the (a) parallel and (b) crossed configurations. The polarized Raman map is a mean to identify the angular behaviour of a specific Raman mode. Spectra in (a) and (b) are unnormalized and share the same scale while maps in (c) and (d) are normalized separately and the intensities are shown in logarithmic scale for better visualization. Author's own work.

located at 175.7 cm^{-1}, 178.9 cm^{-1} and 181.9 cm^{-1} is weakened, where the latter mode is more pronounced in our work (see Fig. 15(b)).

Figures 15 (c) and (d) show the polarized Raman map of both configurations shown in Fig. 15 (a) and (b). The intensity is represented in a logarithmic scale to better visualize the angular dependence of the low-intensity phonon modes. The peak intensity variation of each configuration is clearly observed indicating that the polarized Raman map can be used as a fingerprint to identify specific phonon modes in $ReSe_2$. Similar results are expected to other two-dimensional Re-based TMDs.

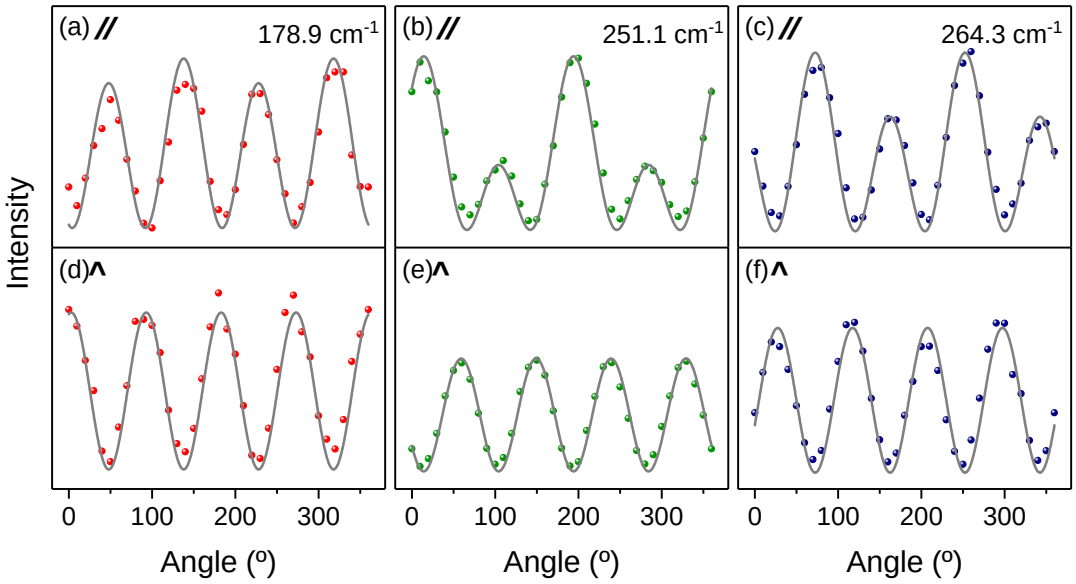

Figure 16 – **Angular dependence for Raman Tensor elements with real values.** Angular dependence of the 178.9 cm^{-1}, 251.1 cm^{-1} and 264.3 cm^{-1} modes (Class I, see text for details) in the (a)–(c) parallel and (d)–(f) crossed configurations. The dots correspond to the experimental data value while solid lines correspond to the adjust according to equations (4.1) using only Raman Tensors with real elements. The data were offset for parallel and crossed configuration of a given mode and scales were modified for better clarity of each mode. Author's own work.

In order to explain the intensity variation between these configurations, we need to consider the polarization vector of the incident and scattered light. In the parallel configuration, the incident and scattered light polarization vectors in our experimental setup are given by $\hat{e}_i = \hat{e}_s = (\cos(\theta), \sin(\theta), 0)$, where θ is the angle that polarization direction with respect to $b-$axis. In the case of the crossed configuration, the polarization vector of the incident and scattered light, respectively, are written as $\hat{e}_i = (-\sin(\theta), \cos(\theta), 0)$ and $\hat{e}_s = (\cos(\theta), \sin(\theta), 0)$. Substituting these expressions in Equation (2.11), we obtain the

following intensity expressions for the parallel ($I_{\parallel}$) and perpendicular ($I_{\perp}$) configurations:

$$I_{\parallel} \propto \left[u\cos^2(\theta) + w\sin^2(\theta) + v\sin(2\theta)\right]^2, \tag{4.1a}$$

$$I_{\perp} \propto \left[(u-w)\left(\frac{1}{2}\sin(2\theta)\right) - v\cos(2\theta)\right]^2. \tag{4.1b}$$

Here we implicitly assumed that the Raman tensor has the form of (2.12), but with only real values. Figure 16 shows the fitting of the experimental data by Eqs. (4.1) for the integrated intensities of the 178.9 cm^{-1}, 251.1 cm^{-1} and 264.3 cm^{-1} modes. The fitting yields good agreement with the experimental data. The fitting process of the parallel and crossed intensities were performed simultaneously with shared parameters (the Raman tensor elements), in order to obtain the correct values for the Raman tensor elements. The experimental error of the measured angles is about 2.5 degrees and 10% is the estimated error for the intensities. We stress that the fits of the experimental data by equations (4.1) were performed considering an unnormalized data taken from the spectra shown in Figure 15.

Although good adjustments were achieved for the 178.9 cm^{-1}, 251.1 cm^{-1} and 264.3 cm^{-1} Raman modes, Eqs. (4.1) does not properly adjust the remaining data set, as shown by the solid gray lines in Figures 17. Note that some Raman modes shown in Figs. 17 and 18 present a similar angular dependence behaviour among themselves, but a distinct angular response from the Raman modes shown in Fig. 16. This result indicates that although all of the 18 modes of the $ReSe_2$ belong to the A_g irreducible representation, they can present distinct angular response due to the different basis functions of the C_i point group for this representation. Therefore, we have grouped the 18 modes of the $ReSe_2$ into four different classes by looking at their similar angular dependencies. The Raman modes shown in Fig. 16 is inserted into class I (Raman tensor fitted by real values), and the ones shown in Figs. 17 and 18 belong to class II, III and IV (Raman tensor fitted by complex values), as indicated in Fig. 18. We stress that three modes (120.1 cm^{-1}, 124.9 cm^{-1} and 197.5 cm^{-1}) belonging to the class III were omitted in Fig. 18 to avoid an oversized picture.

To solve the fitting issue in Fig. 17, we need to consider Raman tensors with complex elements, $\mathbf{u} = ue^{i\phi_u}$, $\mathbf{v} = ve^{i\phi_v}$ and $\mathbf{w} = we^{i\phi_w}$, where u, v, w, ϕ_u, ϕ_v, $\phi_w \in \mathbb{R}$, as

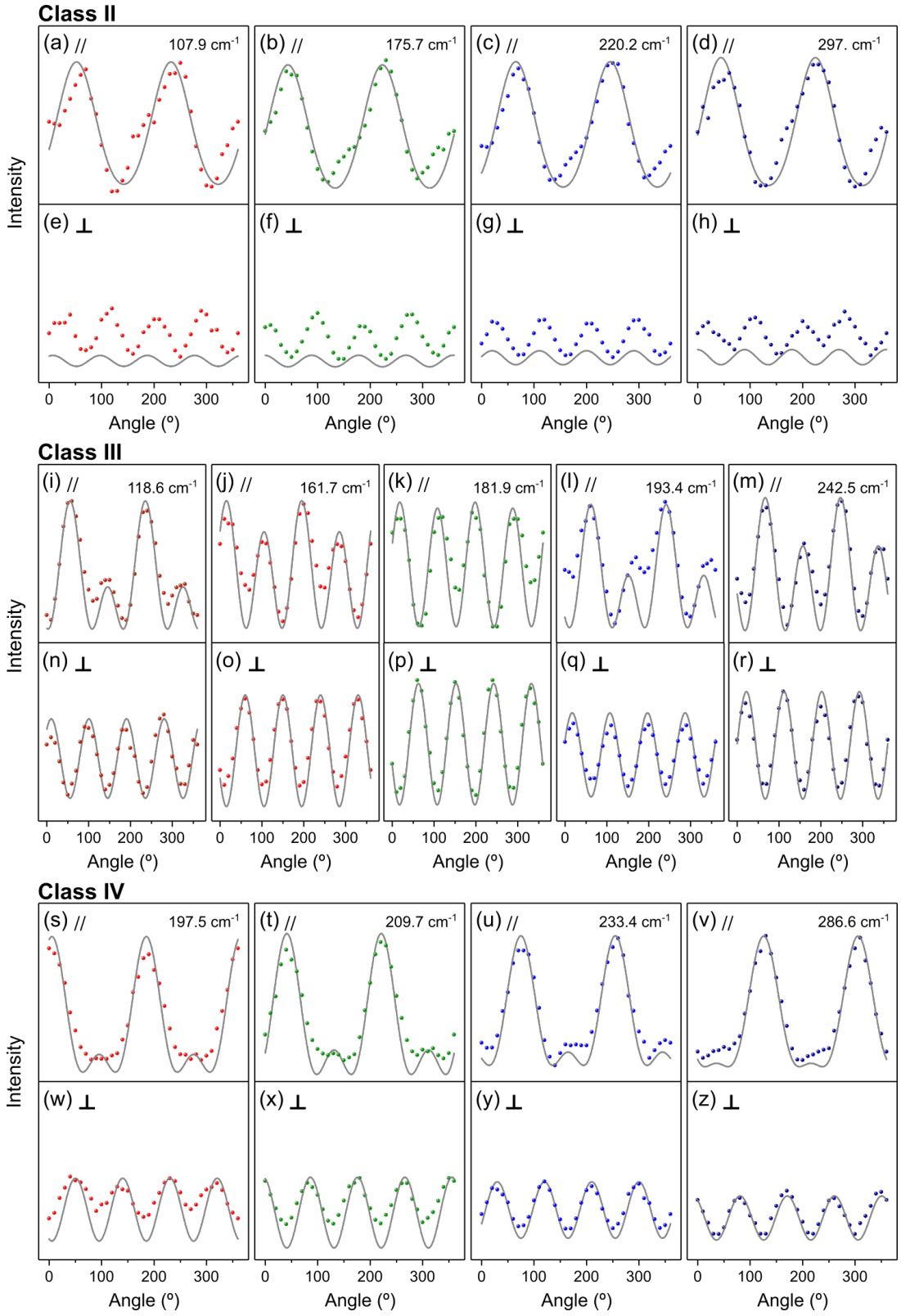

Figure 17 – **Angular dependence of Raman intensities for real Raman Tensor values.** The parallel and crossed configurations of the set Raman modes in 1L-$ReSe_2$ for (a)–(h) Class II, (i)–(r) Class III, (s)–(z) Class IV (see text for details), respectively. Author's own work.

discussed in Chapter 2. Therefore, the expressions (4.1) become:

$$I_{\parallel} \propto u^2\cos^4(\theta) + w^2\sin^4(\theta) + (v\sin(2\theta))^2 + \sin(2\theta)\Bigg(\frac{1}{2}uw\cos(\phi_{uw})\sin(2\theta) + 2uv\cos(\phi_{uv})\cos^2(\theta) + 2wv\cos(\phi_{wv})\sin^2(\theta)\Bigg), \tag{4.2a}$$

$$I_{\perp} \propto \Big(u^2 + w^2 - 2uw\cos(\phi_{uw})\Big)\left(\frac{1}{2}\sin(2\theta)\right)^2 + (v\cos(2\theta))^2 + \frac{1}{2}\sin(4\theta)\Bigg(wv\cos(\phi_{wv}) - uv\cos(\phi_{uv})\Bigg), \tag{4.2b}$$

where $\phi_{ij} = \phi_i - \phi_j$ with i, $j = u$, v, w.

Figure 18 shows the correction of the remaining data set shown in Fig. 17 fitted by Eqs. (4.2). In order to obtain the correct values for the Raman tensor elements, the fitting process in Fig. 18 was also performed simultaneously for both intensity of Eq. (4.2), as similarly done for the modes of Fig. 16.

The previous results show how complex valued Raman tensor elements are essential to most of the Raman active modes of $ReSe_2$. It is noteworthy that the considerable discrepancy of the adjusts between Figs. 17 and 18 are due to the fact that the correct fitting process consists by using Eqs. (4.2) simultaneously with shared parameters. If one tries to fit the crossed configuration intensity ($I_{\perp}$) alone using Eq. (4.1b), it will be seen that all the data set of classes II, III and IV for that configuration would be fitted well without considering complex values for the Raman tensor. However, the Raman tensor elements obtained from this way can not fit the parallel configuration data set when substituted in Eq. (4.1a). To explain this, we need to careful analyze this equation.

From Eq. (4.1b), we observe that the only component of the Raman tensor that can be isolated by twisting the angle of the relative sample's orientation with respect to the incident and scattered light polarization is the off-diagonal component, **v**. It means that the remaining two components (**u** and **w**) become interdependent if we try to adjust the experimental data of only one configuration solely. In this case, these components make up the cosines of the phase differences, misleading to believe that the Raman tensor only possess real components.

In Eq. (2.20), none of the Raman tensor components (**u**, **w** or **v**) can be isolated in any orientation, i.e. all components become interdependent in the fits, masking the effect of the phase differences between the Raman tensor elements in the Raman response for the $ReSe_2$. Table 3 illustrates these considerations by presenting the Raman tensor elements obtained in our work, with the cosines of the phase differences when they are needed. The Raman tensor parameters shown in Table 3 were normalized by the first

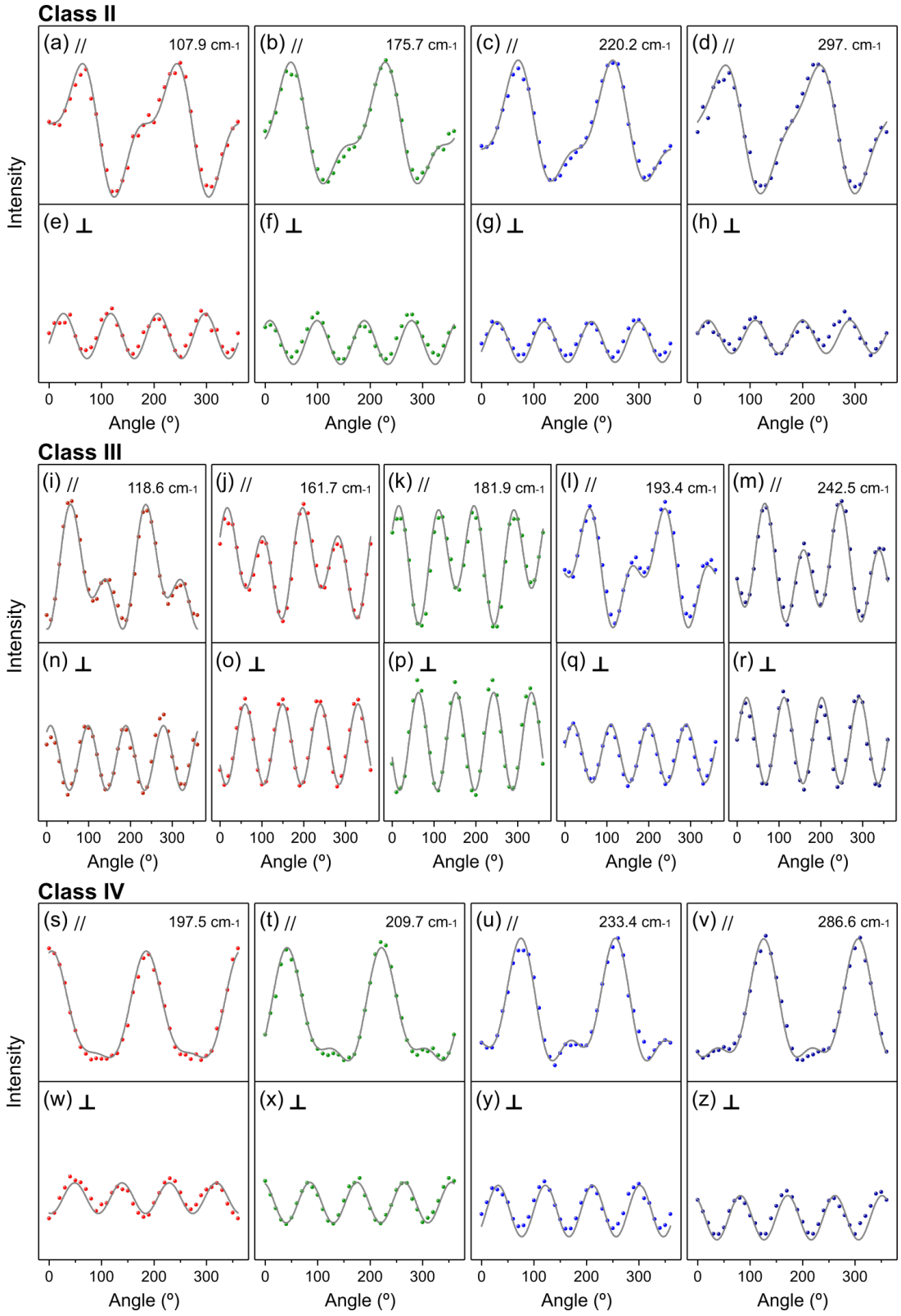

Figure 18 – **Angular dependence of Raman intensities for complex Raman Tensor values.** The parallel and crossed configurations of the set Raman modes in 1L-$ReSe_2$ for (a)–(h) Class II, (i)–(r) Class III, (s)–(z) Class IV (see text for details), respectively. Author's own work.

diagonal component, **u**, where the phase difference ϕ_{wv} is neglected, since it depends on the other two phase differences according to $\phi_{wv} = \phi_{uv} - \phi_{uw}$.

Table 3 – **Raman tensor elements.** Raman tensor elements obtained from the fitting of the experimental data. Pink, red, black and green colors correspond to Class I, II and III, respectively. The dashes in the last column indicates that no complex phases were necessary to fit the experimental data of a respective mode. Author's own work.

Mode (cm^{-1})	v/u	w/u	$\cos(\phi_{uw})$	$\cos(\phi_{uv})$
107.9	0.53411	1.04355	0.11296	-0.05587
118.6	18.38364	16.61875	-0.14742	0.89719
120.1	0.98329	0.73124	0.98358	0.31796
124.9	0.50253	1.10428	0.69677	-0.40152
161.7	0.67052	0.94415	-0.929	-0.7212
175.7	0.71976	0.88164	0.82669	-0.20069
178.9	6.85729	-0.45799	-	-
181.9	0.69716	0.86591	-0.87696	-0.57992
193.4	0.95891	0.96075	-0.42388	0.16846
197.5	0.485	0.39858	-0.96978	-0.16784
209.7	1.29393	0.95247	-0.43747	-0.65538
220.2	0.47519	1.41167	0.29148	-0.10673
233.4	0.72669	2.16127	-0.39153	0.33544
242.5	1.09878	1.20294	-0.9412	0.59477
251.1	-0.42517	-0.56981	-	-
264.3	0.80629	-1.3118	-	-
286.6	1.71231	1.9327	0.92593	0.55941
297.1	0.61167	0.88608	0.32357	-0.23761

Although, the absolute phases cannot be separately measured, their cosines differences show the effect they cause for a given vibrational mode. The closest the modulus of these cosines approaches to 1, less evident will be the phase difference effect. On the other hand, if the modulus approaches to 0, more evident will be the phase difference effect in the Raman response. Moreover, notice that the off-diagonal elements have appreciable modulus for all vibrational modes. This is remarkable since all of them belongs to the A_g irreducible representation, which has null off-diagonal elements for higher symmetries.

The anisotropic properties in the Raman signal response of the $ReSe_2$ can also be highlighted in polar plots, as shown in Figures 19 for the peaks located at 124.9 cm^{-1} and 197.5 cm^{-1}, and in Figure 20 for the remaining 16 vibrational Raman modes. In Fig. 19, we plot the angular dependence of the Raman intensities for the parallel and crossed configurations on the same frame and with the same intensity scale. Recall that $\theta = 0$ is the direction of the $b-$axis and the analyzer placed before the spectrometer entrance. The solid lines correspond to the best fits of each mode (as discussed above) while the symbols correspond to the experimental data. In Fig. 20, the colors represent the Raman modes that belong to the same classes and shown in Table 3 (see above).

To this end, we stress that none of the $ReSe_2$'s Raman modes have its highest intensity in the direction of the crystallographic axes, b (for $\theta = 0°$) and a (for $\theta \approx 119°$), for the parallel configuration. This is an interesting result since it has been reported that the peak at 161.7 cm^{-1} has its highest Raman intensity along the rhenium chains in the bulk regime when measured for an excitation energy of 1.96 eV. Nevertheless, our result is still plausible since the orientation may depend on the excitation laser energy [30].

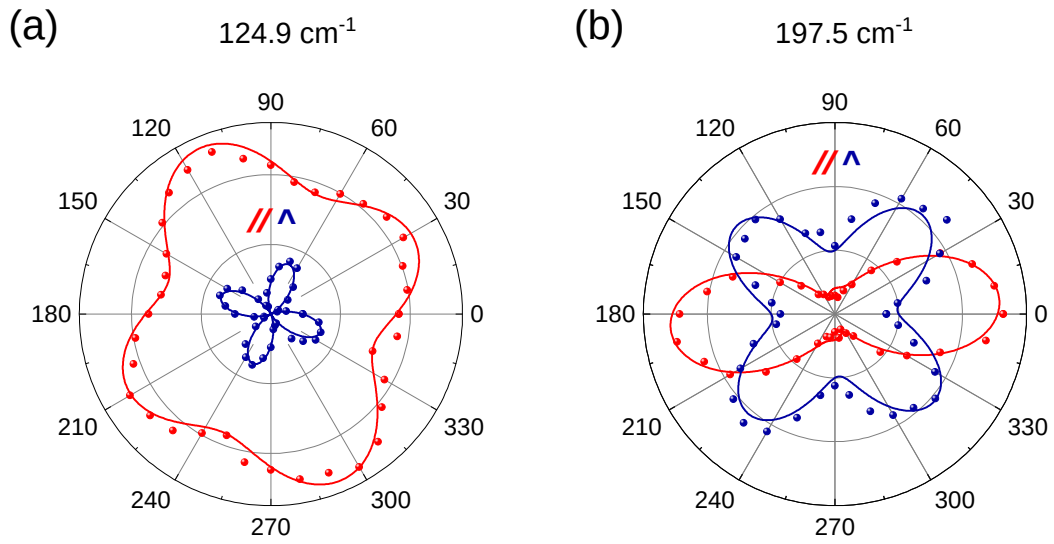

Figure 19 – **Polar plots of two $ReSe_2$ vibration modes.** Polar plots of the (a) 124.9 cm^{-1} and (b) 197.5 cm^{-1} modes. The intensity scale is the for the crossed and perpendicular configurations for a given mode, but it is not the same for different modes. Dots correspond to the experimental data while solid lines correspond to the fits using equations (4.2). Author's own work.

4.3 Conclusion

In summary, in this chapter we presented the angular dependence of the Raman scattering efficiency for the 18 A_g vibrational modes of monolayer $ReSe_2$ in both parallel and crossed configurations. The polarized Raman spectra was measured using the 2.33 eV excitation laser energy and the sample was rotated by 360° in steps of 10°. The unusual dependence of Raman efficiency on the light polarization demonstrates the high anisotropy of the $ReSe_2$ due to its reduced symmetry. This behaviour was explained analytically using the classical approach for the Raman efficiency. Additionally, the angular dependence of few Raman modes was adjusted considering the Raman tensor on the field of real numbers, whereas most of the Raman modes required the Raman tensor on the field of complex numbers. Moreover, none of the them presented its highest intensity in the direction of the crystallographic axes.

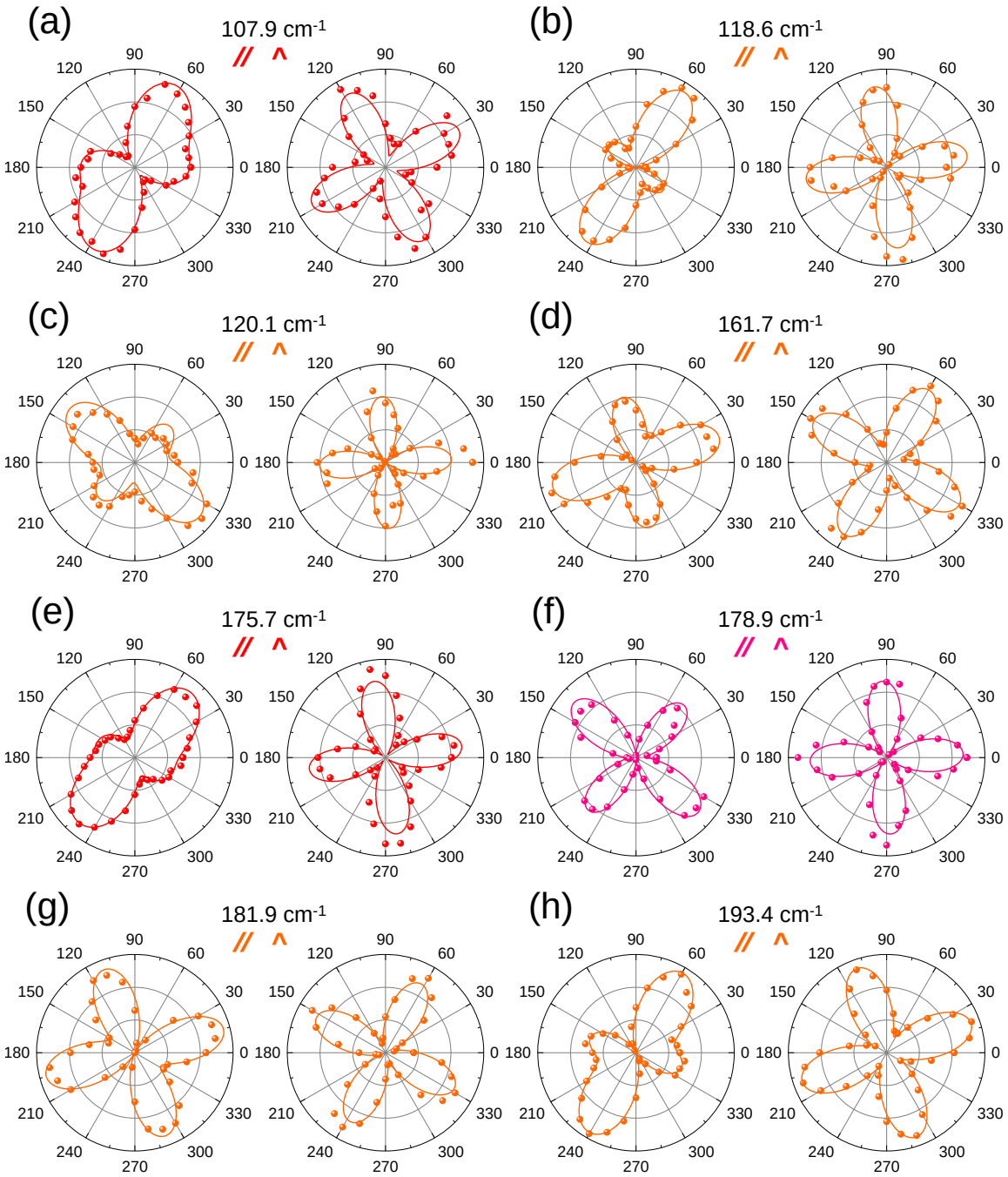
(a)
107.9 cm-1
// ^
(b)
118.6 cm-1
// ^
(c)
120.1 cm-1
// ^
(d)
161.7 cm-1
// ^
(e)
175.7 cm-1
// ^
(f)
178.9 cm-1
// ^
(g)
181.9 cm-1
// ^
(h)
193.4 cm-1
// ^
90 120 60 150 30 180 0 210 330 240 300 270

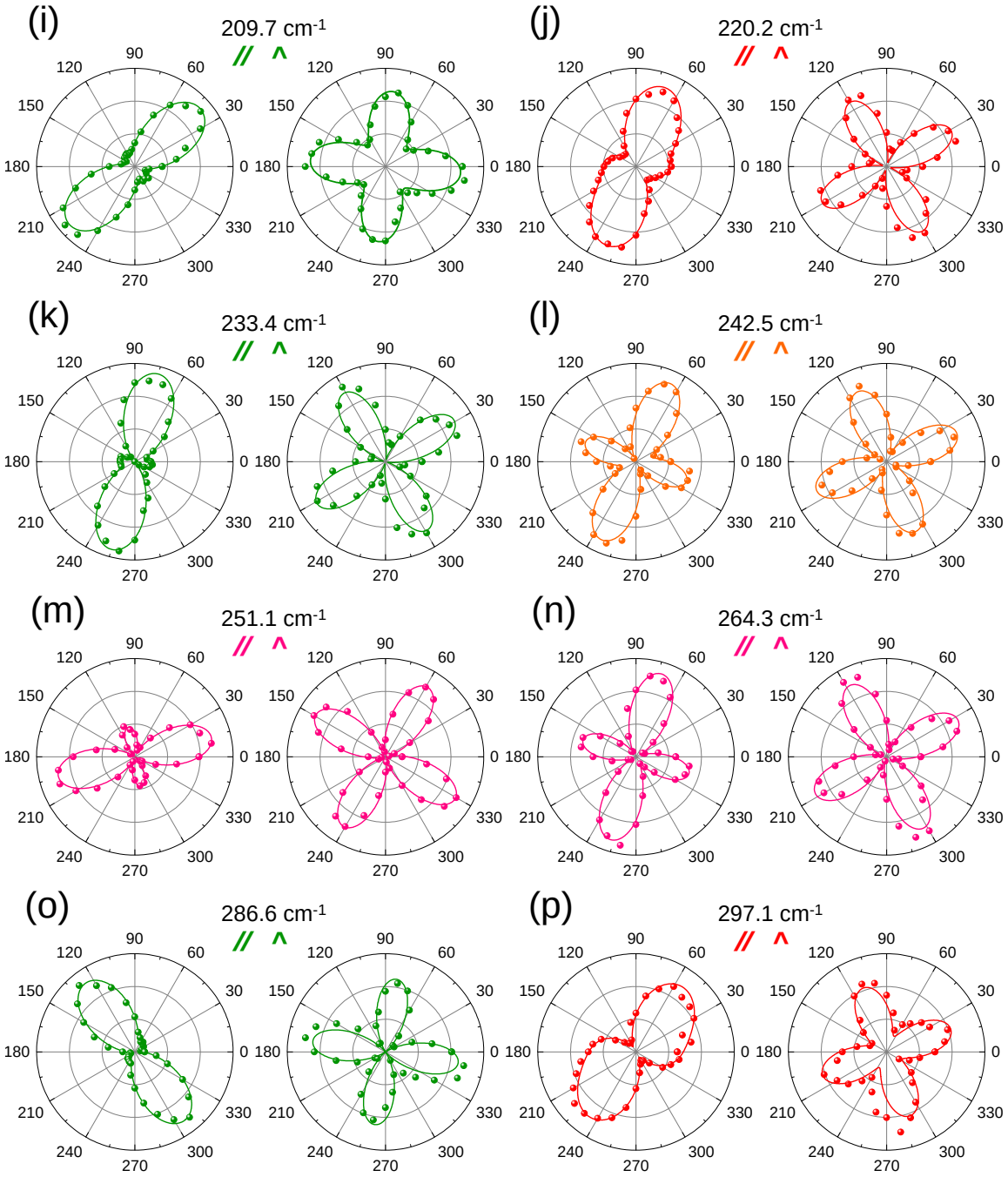

Figure 20 – **Polar plots of $ReSe_2$ vibration modes.** Polar plots of 16 Raman modes in $ReSe_2$. The intensity scale is modified in each plot for better clarity. The dots correspond to the experimental data while solid lines correspond to the fits using appropriate equations for each mode (see text for detail). Colors indicate the class associated with each mode according to Table 3. Author's own work.

Our results shows that the angular dependence of the Raman intensities in single-layer $ReSe_2$ modes are explained considering complex elements for the Raman tensor elements. Therefore, the polarized Raman results reported in the literature for $ReSe_2$ with unpolarized detection does not provide properly information about the electron–photon and electron–phonon interactions in this material. We stress that our results may differ from bulk crystal. Therefore, we avoided comparisons with those results. Our study can also be extended to other Re-based TMDs and 2D systems that possess low-symmetry properties.

Finally, in the classical formalism, the Raman tensor elements have complex values due to the electric susceptibility since they are correlated. On the other hand, the electric susceptibility has complex values only when there is light absorption. Thus, one could suggest that this is also the origin of the complex values for the Raman tensor elements. However, in Eq. 2.19, the effect that comes from the interaction of light with the system is the same for all vibrational modes, which seems to contradict the experimental observations that the phase differences were present for some modes and absent for others. Then, the complex values may have their origins in the electron-phonon interaction since this interaction is unique for each mode. If the latter is the case, would the phase differences remain even if the excitation energy is lower than the band gap of the material? We are still looking for the answer of this question and deeper investigations in the literature are underway.

5 Conclusion and Perspectives

In this Master's thesis, we investigated the anisotropic behaviour of single-layer $ReSe_2$ through polarized Raman spectroscopy. The angular dependence of the polarized Raman spectra for all the 18 A_g modes, predicted by group theory, in both parallel and cross-polarization configurations was measured, and an unusual behavior for the angular dependence of these modes intensities was observed. Our results show that the Raman scattering efficiency presents a distinct angular dependence on the light polarization, and that, for most of the Raman modes, it is necessary to consider Raman tensor with complex elements. This approach allowed us to measure the phase differences between Raman tensor elements for the A_g modes.

To this end, we mention some perspectives for future work on $ReSe_2$. For a further and better understanding of the electron-photon and electron-phonon interaction resonant Raman measurements need to be carry out. This will allow us to gather information on the electronic phases and origin of the optical transitions which is still poorly understood in this material. Additionally, we aim to extend this work for few-layers and bulk $ReSe_2$, which will further provide a classification of the vibrational modes and a reliable method to find the crystallographic orientation of the samples.

Bibliography

[1] K. S. Novoselov, A. K. Geim, S. V. Morozov, D. Jiang, Y. Zhang, S. V. Dubonos, I. V. Grigorieva, and A. A. Firsov. Electric field effect in atomically thin carbon films. *Science*, 306(5696):666–669, 2004. Citado na página 11.

[2] P. Miro, M. Audiffred, and T. Heine. An atlas of two-dimensional materials. *Chem. Soc. Rev.*, 43:6537–6554, 2014. Citado na página 11.

[3] A. K. Geim and I. V. Grigorieva. Van der waals heterostructures. *Nature*, 499:419 EP –, Jul 2013. Perspective. Citado 3 vezes nas páginas 11, 12, and 28.

[4] J.A. Wilson and A.D. Yoffe. The transition metal dichalcogenides discussion and interpretation of the observed optical, electrical and structural properties. *Advances in Physics*, 18(73):193–335, 1969. Citado 2 vezes nas páginas 11 and 13.

[5] R. Lv, J. A. Robinson, R. E. Schaak, D. Sun, Y. Sun, T. E. Mallouk, and M. Terrones. Transition metal dichalcogenides and beyond: Synthesis, properties, and applications of single- and few-layer nanosheets. *Accounts of Chemical Research*, 48(1):56–64, 2015. PMID: 25490673. Citado 2 vezes nas páginas 11 and 28.

[6] N. Mounet, M. Gibertini, P. Schwaller, D. Campi, A. Merkys, A. Marrazzo, T. Sohier, I. E. Castelli, A. Cepellotti, G. Pizzi, and N. Marzari. Two-dimensional materials from high-throughput computational exfoliation of experimentally known compounds. *Nature Nanotechnology*, 13(3):246, 2018. Citado na página 11.

[7] Q. H. Wang, K. Kalantar-Zadeh, A. Kis, J. N. Coleman, and M. S. Strano. Electronics and optoelectronics of two-dimensional transition metal dichalcogenides. *Nature Nanotechnology*, 7(11):699–712, 2012. Citado na página 11.

[8] S. Tongay, S. S. Varnoosfaderani, B. R. Appleton, J. Wu, and A. F. Hebard. Magnetic properties of MoS_2: existence of ferromagnetism. *Applied Physics Letters*, 101(12):123105, 2012. Citado na página 11.

[9] S. Mathew, K. Gopinadhan, T. K. Chan, X. J. Yu, D. Zhan, L. Cao, A. Rusydi, M. B. H. Breese, S. Dhar, Z. X. Shen, T. Venkatesan, and J. T. L. Thong. Magnetism in MoS_2 induced by proton irradiation. *Applied Physics Letters*, 101(10):102103, 2012. Citado na página 11.

[10] K. S. Novoselov, D. Jiang, F. Schedin, T. J. Booth, V. V. Khotkevich, S. V. Morozov, and A. K. Geim. Two-dimensional atomic crystals. *Proceedings of the National*

Academy of Sciences of the United States of America, 102(30):10451–10453, 2005. Citado 2 vezes nas páginas 11 and 28.

[11] A. Splendiani, L. Sun, Y. Zhang, T. Li, J. Kim, C. Chim, G. Galli, and F. Wang. Emerging photoluminescence in monolayer MoS_2. *Nano Letters*, 10(4):1271–1275, 2010. PMID: 20229981. Citado 2 vezes nas páginas 11 and 12.

[12] K. F. Mak, C. Lee, J. Hone, J. Shan, and T. F. Heinz. Atomically thin MoS_2: A new direct-gap semiconductor. *Phys. Rev. Lett.*, 105:136805, Sep 2010. Citado 2 vezes nas páginas 11 and 12.

[13] Y. Lee, X. Zhang, W. Zhang, M. Chang, C. Lin, K. Chang, Y. Yu, J. T. Wang, C. Chang, L. Li, and T. Lin. Synthesis of large-area MoS_2 atomic layers with chemical vapor deposition. *Advanced Materials*, 24(17):2320–2325, 2012. Citado na página 11.

[14] G. Eda, H. Yamaguchi, D. Voiry, T. Fujita, M. Chen, and M. Chhowalla. Photoluminescence from chemically exfoliated mos2. *Nano Letters*, 11(12):5111–5116, 2011. PMID: 22035145. Citado na página 11.

[15] W. S. Yun, S. W. Han, S. C. Hong, I. G. Kim, and J. D. Lee. Thickness and strain effects on electronic structures of transition metal dichalcogenides: $2H - MX_2$ semiconductors (m = mo, w; x = s, se, te). *Phys. Rev. B*, 85:033305, Jan 2012. Citado na página 12.

[16] X. Zhang, X. Qiao, W. Shi, J. Wu, D. Jiang, and P. Tan. Phonon and Raman scattering of two-dimensional transition metal dichalcogenides from monolayer, multilayer to bulk material. *Chemical Society Reviews*, 44:2757–2785, 2015. Citado na página 12.

[17] Z. Y. Zhu, Y. C. Cheng, and U. Schwingenschlögl. Giant spin-orbit-induced spin splitting in two-dimensional transition-metal dichalcogenide semiconductors. *Phys. Rev. B*, 84:153402, Oct 2011. Citado na página 12.

[18] X. Xu, W. Yao, D. Xiao, and T. F. Heinz. Spin and pseudospins in layered transition metal dichalcogenides. *Nature Physics*, 10(5):343–350, 05 2014. Copyright - Copyright Nature Publishing Group May 2014; Última atualização em - 2014-11-21. Citado na página 12.

[19] H. Li, Q. Zhang, C. C. R. Y., B. K. Tay, T. H. T. Edwin, A. Olivier, and D. Baillargeat. From bulk to monolayer MoS_2: Evolution of raman scattering. *Advanced Functional Materials*, 22(7):1385–1390, 2012. Citado 2 vezes nas páginas 12 and 29.

[20] B. Radisavljevic, A. Radenovic, J. Brivio, V. Giacometti, and A. Kis. Single-layer MoS_2 transistors. *Nat Nano*, 6(3):147–150, Mar 2011. Citado na página 12.

[21] D. Kufer and G. Konstantatos. Highly sensitive, encapsulated MoS_2 photodetector with gate controllable gain and speed. *Nano Letters*, 15(11):7307–7313, 2015. PMID: 26501356. Citado na página 12.

[22] Bruno Ricardo de Carvalho. *Raman Spectroscopy in MoS_2-Type Transition-Metal Dichalcogenides*. PhD thesis, Universidade Federal de Minas Gerais, Fevereiro 2017. Citado 2 vezes nas páginas 13 and 21.

[23] E. Zhang, P. Wang, Z. Li, H. Wang, C. Song, C. Huang, Z. Chen, L. Yang, K. Zhang, S. Lu, W. Wang, S. Liu, H. Fang, X. Zhou, H. Yan, J. Zou, X. Wan, P. Zhou, W. Hu, and F. Xiu. Tunable ambipolar polarization-sensitive photodetectors based on high-anisotropy $ReSe_2$ nanosheets. *ACS Nano*, 10(8):8067–8077, 2016. PMID: 27472807. Citado na página 12.

[24] S. Yang, S. Tongay, Y. Li, Q. Yue, J. Xia, S. Li, J. Li, and S. Wei. Layer-dependent electrical and optoelectronic responses of $ReSe_2$ nanosheet transistors. *Nanoscale*, 6:7226–7231, 2014. Citado na página 12.

[25] Shengxue Yang, Cong Wang, Hasan Sahin, Hui Chen, Yan Li, Shu-Shen Li, Aslihan Suslu, Francois M. Peeters, Qian Liu, Jingbo Li, and Sefaattin Tongay. Tuning the optical, magnetic, and electrical properties of rese2 by nanoscale strain engineering. *Nano Letters*, 15(3):1660–1666, 2015. PMID: 25642738. Citado na página 13.

[26] D. Wolverson, S. Crampin, A. S. Kazemi, A. Ilie, and S. J. Bending. Raman spectra of monolayer, few-layer, and bulk $ReSe_2$: An anisotropic layered semiconductor. *ACS Nano*, 8(11):11154–11164, 2014. PMID: 25365239. Citado 8 vezes nas páginas 13, 14, 23, 24, 28, 29, 35, and 36.

[27] H. Zhao, J. Wu, H. Zhong, Q. Guo, X. Wang, F. Xia, L. Yang, P. Tan, and H. Wang. Interlayer interactions in anisotropic atomically thin rhenium diselenide. *Nano Research*, 8(11):3651–3661, Nov 2015. Citado 6 vezes nas páginas 13, 14, 23, 24, 28, and 29.

[28] H.-J. Lamfers, A. Meetsma, G.A. Wiegers, and J.L. de Boer. The crystal structure of some rhenium and technetium dichalcogenides. *Journal of Alloys and Compounds*, 241(1):34 – 39, 1996. Citado na página 13.

[29] . Jariwala, A. Thamizhavel, and A. Bhattacharya. $ReSe_2$: a reassessment of crystal structure and thermal analysis. *Journal of Physics D: Applied Physics*, 50(4):044001, 2017. Citado 2 vezes nas páginas 13 and 14.

[30] E. Lorchat, G. Froehlicher, and S. Berciaud. Splitting of interlayer shear modes and photon energy dependent anisotropic raman response in n-layer $ReSe_2$ and ReS_2. *ACS*

Nano, 10(2):2752–2760, 2016. PMID: 26820232. Citado 8 vezes nas páginas 13, 23, 24, 25, 28, 29, 30, and 44.

[31] C. V. Raman and K. S. Krishnan. A new type of secondary radiation. *Nature*, 121(3048):501, 1928. Citado na página 16.

[32] The nobel prize in physics 1930. `https://www.nobelprize.org/nobel_prizes/physics/laureates/1930/raman-facts.html`. Acccessed: 01 June, 2018. Citado na página 16.

[33] J.R. Ferraro, K. Nakamoto, and C.W. Brown. *Introductory Raman Spectroscopy*. Elsevier, second edition, 2003. Citado 2 vezes nas páginas 16 and 18.

[34] P.Y. Yu and M. Cardona. *Fundamentals of semiconductors*. Springer-Verlag Berlin Heidelberg, fourth edition, 2010. Citado 4 vezes nas páginas 16, 18, 20, and 22.

[35] D. L Andrews. Raman scattering and spectral interpretation. In *Molecular Photophysics and Spectroscopy*, 2053-2571, pages 8–1 to 8–10. Morgan & Claypool Publishers, 2014. Citado na página 18.

[36] T. Strach, J. Brunen, B. Lederle, J. Zegenhagen, and M. Cardona. Determination of the phase difference between the raman tensor elements of the A_{1g}-like phonons in $SmBa_2Cu_3O_{7-\delta}$. *Phys. Rev. B*, 57:1292–1297, Jan 1998. Citado na página 19.

[37] H. B. Ribeiro, Ma. A. Pimenta, C. J. S. de Matos, R. L. Moreira, A. S. Rodin, J.D. Zapata, E. A. T. de Souza, and A.H. Castro Neto. Unusual angular dependence of the raman response in black phosphorus. *ACS Nano*, 9(4):4270–4276, 2015. PMID: 25752593. Citado na página 19.

[38] Q. Song, X. Pan, H. Wang, K. Zhang, Q. Tan, P. Li, Y. Wan, Y. Wang, X. Xu, M. Lin, X. Wan, F. Song, and L. Dai. The In-Plane Anisotropy of WTe_2 Investigated by Angle-Dependent and Polarized Raman Spectroscopy. *Scientific Reports*, 6:1–9, 2016. Citado na página 19.

[39] Q. Song, H. Wang, X. Pan, X. Xu, Y. Wang, Y. Li, F. Song, X. Wan, Y. Ye, and L. Dai. Anomalous in-plane anisotropic Raman response of monoclinic semimetal 1T-MoTe2_2. *Scientific Reports*, 7(1):1–10, 2017. Citado na página 19.

[40] L.D. Landau and E.M. Lifshitz. *Statistical Physics*. Butterworth-Heinemann, third edition, 1980. Citado na página 19.

[41] L.D. Landau, L.P. Pitaevskii, and E.M. Lifshitz. *Electrodynamics of Continuous Media*. Butterworth-Heinemann, second edition, 1984. Citado na página 19.

[42] R. Loudon. The raman effect in crystals. *Advances in Physics*, 50(7):813–864, 2001. Citado na página 19.

[43] R. Loudon. Theory of the first-order raman effect in crystals. *Proceedings of the Royal Society of London A: Mathematical, Physical and Engineering Sciences*, 275(1361):218–232, 1963. Citado na página 20.

[44] R. Loudon. *The quantum theory of light*. Clarendon Press, 1973. Citado na página 21.

[45] C. Kranert, C. Sturm, R. Schmidt-Grund, and M. Grundmann. Raman tensor formalism for optically anisotropic crystals. *Phys. Rev. Lett.*, 116:127401, Mar 2016. Citado na página 24.

[46] S. Zhang, N. Mao, N. Zhang, J. Wu, L. Tong, and J. Zhang. Anomalous Polarized Raman Scattering and Large Circular Intensity Differential in Layered Triclinic ReS_2. *ACS Nano*, 11(10):10366–10372, 2017. Citado 3 vezes nas páginas 24, 25, and 27.

[47] L. Hart, S. Dale, S. Hoye, J. L. Webb, and D. Wolverson. Rhenium Dichalcogenides: Layered Semiconductors with Two Vertical Orientations. *Nano Letters*, 16(2):1381–1386, 2016. Citado 5 vezes nas páginas 25, 26, 28, 29, and 30.

[48] H. Muhammad, G. Lin, L. Huiqiao, M. Ying, and Z. Tianyou. Chemical vapor deposition synthesis of ultrathin hexagonal $ReSe_2$ flakes for anisotropic raman property and optoelectronic application. *Advanced Materials*, 28(37):8296–8301, 2016. Citado na página 28.

[49] F. Cui, X. Li, Q. Feng, J. Yin, L. Zhou, D. Liu, K. Liu, X. He, X. Liang, S. Liu, Z. Lei, Z. Liu, H. Peng, J. Zhang, J. Kong, and H. Xu. Epitaxial growth of large-area and highly crystalline anisotropic $ReSe_2$ atomic layer. *Nano Research*, 10(8):2732–2742, Aug 2017. Citado na página 28.

[50] S. Jiang, Z. Zhang, N. Zhang, Y. Huan, Y. Gong, M. Sun, J. Shi, C. Xie, P. Yang, Q. Fang, He Li, L. Tong, D. Xie, L. Gu, P. Liu, and Y. Zhang. Application of chemical vapor–deposited monolayer $ReSe_2$ in the electrocatalytic hydrogen evolution reaction. *Nano Research*, 11(4):1787–1797, Apr 2018. Citado na página 28.

[51] The nobel prize in physis 2010. `https://www.nobelprize.org/nobel_prizes/physics/laureates/2010/`. Accessed: 2018-05-11. Citado na página 28.

[52] M. Yi and Z. Shen. A review on mechanical exfoliation for the scalable production of graphene. *J. Mater. Chem. A*, 3:11700–11715, 2015. Citado 2 vezes nas páginas 28 and 29.

[53] I. Jung, M. Pelton, R. Piner, D. A. Dikin, S. Stankovich, S. Watcharotone, M. Hausner, and R. S. Ruoff. Simple approach for high-contrast optical imaging and characterization of graphene-based sheets. *Nano Letters*, 7(12):3569–3575, 2007. Citado na página 29.

[54] M. A. Pimenta, E. del Corro, B. R. Carvalho, C. Fantini, and L. M. Malard. Comparative study of raman spectroscopy in graphene and mos_2-type transition metal dichalcogenides. *Accounts of Chemical Research*, 48(1):41–47, 2015. PMID: 25490518. Citado na página 29.

[55] A. C. Ferrari and D. M. Basko. Raman spectroscopy as a versatile tool for studying the properties of graphene. *Nature Nanotechnology*, 8:235 EP –, Apr 2013. Review Article. Citado na página 29.

[56] X. Zhang, X. Qiao, W. Shi, J. Wu, D. Jiang, and P. Tan. Phonon and raman scattering of two-dimensional transition metal dichalcogenides from monolayer, multilayer to bulk material. *Chem. Soc. Rev.*, 44:2757–2785, 2015. Citado na página 29.

[57] B. R. Carvalho, Y. Hao, A. Righi, J. F. Rodriguez-Nieva, L. Colombo, R. S. Ruoff, M. A. Pimenta, and C. Fantini. Probing carbon isotope effects on the raman spectra of graphene with different ^{13}C concentrations. *Phys. Rev. B*, 92:125406, Sep 2015. Citado na página 29.

[58] A. Das, S. Pisana, B. Chakraborty, S. Piscanec, S. K. Saha, U. V. Waghmare, K. S. Novoselov, H. R. Krishnamurthy, A. K. Geim, A. C. Ferrari, and A. K. Sood. Monitoring dopants by raman scattering in an electrochemically top-gated graphene transistor. *Nature Nanotechnology*, 3:210 EP –, Mar 2008. Citado na página 29.

[59] S. Mignuzzi, A.J. Pollard, N. Bonini, B. Brennan, I. S. Gilmore, M. A. Pimenta, D. Richards, and D. Roy. Effect of disorder on raman scattering of single-layer Mos_2. *Phys. Rev. B*, 91:195411, May 2015. Citado na página 29.

[60] H. Zeng, B. Zhu, K. Liu, J. Fan, and Q. M. Cui, X.and Zhang. Low-frequency raman modes and electronic excitations in atomically thin mos_2 films. *Phys. Rev. B*, 86:241301, Dec 2012. Citado na página 29.

[61] Luciano de Moura Guimarães. *Perfis de espalhamento Raman ressonante em estruturas unidimensionais de carbono: cadeias lineares e nanotubos quiralmente enriquecidos*. PhD thesis, Universidade Federal de Minas Gerais, Dezembro 2011. Citado na página 31.